RESEARCH ARTICLE | NOVEMBER 18 2024

Calibration of MAJIS (Moons and Jupiter Imaging Spectrometer). IV. Radiometric calibration (invited)

Special Collection: Performances of the Moons And Jupiter Imaging Spectrometer on Board the Juice Spacecraft

Y. Langevin ; F. Poulet; G. Piccioni ; G. Filacchione ; C. Dumesnil ; F. Tosi ; J. Carter ; A. Barbis; P. Haffoud ; L. Tommasi; M. Vincendon ; S. De Angelis ; I. Guerri; C. Pilorget ; S. Rodriguez ; S. Stefani ; D. Bolsée ; M. Cisneros ; L. Van Laeken; N. Pereira ; A. Carapelle

Rev. Sci. Instrum. 95, 111301 (2024)
https://doi.org/10.1063/5.0202702

Review of Scientific Instruments ARTICLE pubs.aip.org/aip/rsi

Calibration of MAJIS (Moons and Jupiter Imaging Spectrometer). IV. Radiometric calibration (invited)

Cite as: Rev. Sci. Instrum. 95, 111301 (2024); doi: 10.1063/5.0202702
Submitted: 6 February 2024 • Accepted: 14 October 2024 •
Published Online: 18 November 2024

Y. Langevin,[1,a)] F. Poulet,[1] G. Piccioni,[2] G. Filacchione,[2] C. Dumesnil,[1] F. Tosi,[2] J. Carter,[1] A. Barbis,[3] P. Haffoud,[1] L. Tommasi,[3] M. Vincendon,[1] S. De Angelis,[2] I. Guerri,[3] C. Pilorget,[1] S. Rodriguez,[4] S. Stefani,[2] D. Bolsée,[5] M. Cisneros,[5] L. Van Laeken,[5] N. Pereira,[5] and A. Carapelle[6]

AFFILIATIONS

[1] Institut d'Astrophysique Spatiale, CNRS-Université Paris-Saclay, Orsay 91400, France
[2] Istituto di Astrofisica e Planetologia Spaziali, Istituto Nazionale di Astrofisica, Rome 00133, Italy
[3] Leonardo Company, via delle Officine Galileo, 1, Campi Bisenzio 50013, Italy
[4] Institut de Physique du Globe de Paris, CNRS-Université Paris-Cité, Paris 75005, France
[5] Royal Belgian Institute for Space Aeronomy Av. Circulaire 3, 1180 Brussels, Belgium
[6] Centre Spatial de Liège - Université de Liège, Avenue du Pré-Aily, B-4031 Angleur-Liège, Belgium

Note: Paper published as part of the Special Topic on Performances of the Moons and Jupiter Imaging Spectrometer on Board the Juice Spacecraft.
[a)]**Author to whom correspondence should be addressed:** yves.langevin@ias.u-psud.fr

ABSTRACT

The MAJIS (Moons and Jupiter Imaging Spectrometer) instrument is an imaging spectrometer on-board the JUICE (JUpiter ICy moons Explorer) spacecraft. MAJIS covers the spectral range from 0.5 to 5.54 μm with two channels [visible–near infrared (VISNIR) and IR]. A comprehensive campaign of on-ground MAJIS calibration was conducted in August and September 2021 in the IAS (Institut d'Astrophysique Spatiale, CNRS/Université Paris-Saclay) facilities. In this article, we present the results relevant for the radiometric calibration of MAJIS. Due to the specific characteristics of the MAJIS detectors (H1RG from Teledyne), an extensive detector characterization campaign was implemented for both the VISNIR and IR detectors before integration so as to validate readout procedures providing precision and accuracy. The characterization also provided critical information on linearity and operability as a function of the integration time and operating temperature. The radiometric calibration of the integrated MAJIS instrument focused on the determination of the instrument transfer function in terms of DN output per unit of radiance for each MAJIS data element as a function of its position in the field of view of MAJIS and its central wavelength. The radiometric calibration of the VISNIR channel required a specific procedure due to stray light at short wavelengths. Observations of an internal calibration source during calibration and after launch (April 14, 2023) showed that there were minor changes in both the VISNIR and IR channels. The instrument transfer functions to be used in flight have been updated on this basis.

I. INTRODUCTION

Moons And Jupiter Imaging Spectrometer (MAJIS) is the visible–near infrared (VISNIR) imaging spectrometer of the JUpiter ICy moons Explorer (JUICE) mission (wavelength range: 0.49–5.56 μm) dedicated to the study of Jupiter and its system. A detailed description of the science objectives of MAJIS is provided in Ref. 1. Medium and high-resolution observations of the three icy Galilean moons (Europa, Ganymede, and Callisto) will be obtained during two close flybys (Europa), 21 close flybys (Callisto), 8 close flybys and a 280-day long orbital phase (Ganymede). The atmosphere of Jupiter will be observed at intervals of a few days over a wide range of distances and phase angles during the 3.4 year long tour from Jupiter Orbit Insertion (JOI) to Ganymede Orbit Insertion

(GOI). Exospheres, rings, Io, and small satellites will also be observed during the 4 year long science mission.

As is mandatory for payload instruments on planetary science missions, after a proprietary period of 6 months, the MAJIS PI team must make available all the collected data in physical units (radiances for imaging spectrometers such as MAJIS) to the science community, which can from then on publish scientific articles independently from the PI team. It is therefore essential that the science community is made aware of the numerous issues that can impact the interpretation of MAJIS data (operability, linearity, smile and keystone, stray light, "spikes" resulting from high energy electrons in the Jupiter system, etc.). For this purpose, the MAJIS team has prepared a series of six articles in "Review of Scientific Instruments" presenting the MAJIS calibration setup,[2] results on the spatial calibration,[3] the spectral calibration,[4] observations of representative samples,[5] and the internal calibration unit.[6] In this article, we present the results relevant for the radiometric calibration of MAJIS.

A. Specific characteristics of MAJIS relevant for radiometric calibration

MAJIS will investigate the spectral characteristics of Jupiter, the Galilean satellites, rings, small satellites, and exospheres with two channels: the VISNIR channel (0.5–2.35 μm) and the IR channel (2.28–5.54 μm). A beam splitter in the optical head (OH) sends short and long wavelength photons to two grating spectrometers. Photons going through a slit defining the MAJIS field of view (FOV) (0.06 rad) and instantaneous field of view (IFOV) (150 μrad) are projected by the grating onto the detector so that the along-slit direction is spatial and the across-slit direction is spectral (see Ref. 1 for a detailed description of the optical design of MAJIS). Thanks to advances in IR detectors and on-board processing since the early 1980s, the data collection rate of MAJIS is 10 000 times larger than that of NIMS, the VISNIR imaging spectrometer of Galileo, a NASA mission that performed 34 flybys of Jupiter satellites.

A H1RG detector from Teledyne (1024 × 1024 pixels, 18 μm pitch) has been selected as the Focal Plane Array (FPA) for both MAJIS channels as the detection of very low signals is of interest for major science goals of MAJIS (exospheres, Jupiter auroras, rings, and deep absorption bands of H_2O ice in Europa or Ganymede spectra). The HxRG family of detectors has been already used for ground-based astronomy and for the focal planes of space astrophysics missions (e.g., JWST[7] and Euclid[8]) due to its excellent performance at very low signal levels (down to a few e^-). The composition of the HgCdTe sensitive layer has been adjusted for the best performance in the relevant spectral range for each channel. This performance for low signals is obtained by reading out in parallel 16 channels (each 64 pixels wide) and converting them to DNs with a 16-bit analog-to-digital converter (ADC) operating at 100 kHz.[9] For MAJIS, readout and conversion are performed using a SIDECAR ASIC from Teledyne [Focal Plane Electronics (FPE)].

The H1RG detector and its implementation for the VISNIR and IR channels of MAJIS are presented in Fig. 1. The nominal IFOV of MAJIS (150 μrad) and spectral sampling (~3.6 μm for the VISNIR channel and ~6.5 nm for the IR channel[4]) is obtained by averaging data from a 2 × 2 square of H1RG pixels (18 × 18 μm^2). Therefore, with nominal sampling, the VISNIR and IR spectral ranges are each

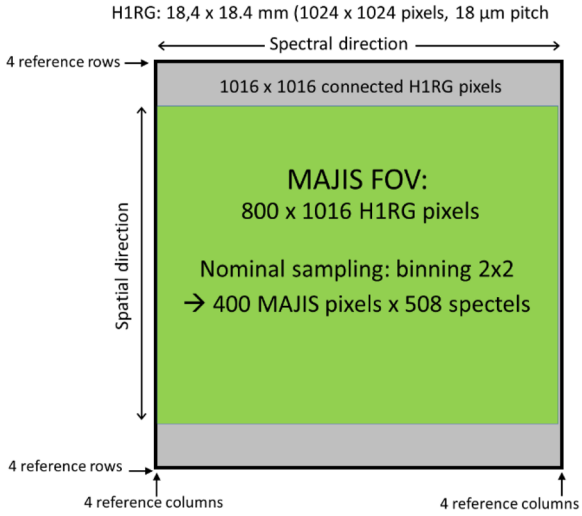

FIG. 1. H1RG detector as used by MAJIS. Four rows and columns along each edge of the detector are not connected to the sensitive layer (reference pixels). The MAJIS grating projects photons from a given location in the FOV along detector rows (spectral direction), the spatial direction being aligned with detector columns.

covered by 508 spectels.[4] The FOV of MAJIS is 3.6°, 400 MAJIS pixels,[3] corresponding to a window of 800 of the 1016 detector rows connected to the sensitive layer.

MAJIS observations cover a very wide dynamic range, with near-saturation levels obtained for bright targets (icy surfaces in the visible range and Jupiter hot spots in the IR range) in less than 200 ms over part of the wavelength range, with signals up to a factor 10 000 higher than low signal levels. This led to implement both the standard 100 kHz readout mode for low signals/long integration times and a 1 MHz readout mode, which was developed specifically for MAJIS for reading out the full projected MAJIS FOV (800 H1RG pixel rows out of 1024) in less than 100 ms as required for short dwell times (high resolution observations of icy moons) or high collection rates (Jupiter and icy satellites in the VISNIR range and Jupiter hot spots in the IR range) so as to avoid saturation.

Coping with a reset anomaly requires comparing signal levels from an HxRG on a series of acquisitions after reset.[9] MAJIS implements "Correlated Double Sampling" (CDS), the signal being obtained by subtracting the DN levels on two acquisitions, one obtained immediately after reset and the other obtained after the integration time selected by TC. Due to the decrease in the transimpedance ($\mu V/e^-$) with the signal level,[9,10] the HxRG detectors are intrinsically not linear. Furthermore, a few percentage of the signal from a given 18 μm pixel is provided by its four nearest neighbor H1RG pixels.[11,12]

Even with CDS, the signal levels from the 8 H1RG pixels unconnected to the sensitive layer at the beginning and end of each row must be used as a reference for the 1016 pixels that are connected to the sensitive layer. There are also four reference rows along the bottom and top edge of the detector, but they are not available for MAJIS when implementing nominal science observations as only the 800 central rows corresponding to the MAJIS FOV are read out.

A H1RG readout procedure specific to MAJIS[13] has been defined for both the 100 kHz and 1 MHz readout operating modes to obtain accuracy with a near optimum performance down to very small signal levels (a few e^-) without relying on reference rows. It requires dark current subtraction even when the dark current level is small (VISNIR FPA), which is performed on the fly by the MAJIS proximity electronics (PE).

Last but not least, coping with the high radiation noise expected when close to Jupiter also required specific on-board de-spiking procedures. They rely on readout procedures being free of persistence, with no significant impact of a spike impacting a given data element on the following acquisition of the same data element.

B. MAJIS radiometric calibration approach and objectives

As for all previously flown imaging spectrometers, the science return of MAJIS is critically dependent on the reliability of its radiometric calibration, which makes it possible to determine the radiance in $W/\mu m/m^2/str$ for a given pixel and wavelength from the Digital Number (DN) level of the corresponding data element. Such information could have been obtained after integration of the proto-flight model by using radiometrically calibrated sources. However, the specific characteristics of the MAJIS detectors led to proceed in two steps: detector characterization and radiometric calibration of the integrated MAJIS instrument.

On this basis, the MAJIS team implemented an extensive characterization campaign of the flight and spare detectors (one each for each channel) before integrating them into the focal plane units of the MAJIS optical head (OH). A first set of tests was performed by Teledyne before delivery at the nominal operating temperature of the VISNIR FPA (140 K) and the IR FPA (90 K). The characterization of the VISNIR detectors[14,15] was performed at IASB (Brussels, Belgium). The characterization of the IR detectors[16] was performed at IAS (Orsay, France). Persistence tests using radioactive sources were performed with a reject grade detector and later on with an EM grade detector at CSL Liège (Belgium). For characterization, the detector was read out at both 100 kHz and 1 MHz with external signal levels ranging from 0 ("dark current") to saturation with a set of detector temperatures (125–140 K for the VISNIR channel and 75–105 K for the IR channel) covering (with margins) the expected operating range of the corresponding MAJIS channel. The characterization campaigns were implemented at the H1RG pixel level (18 μm pitch, 1016 × 1016 connected pixels) before integrating the filters on the FPAs [high pass Linear Variable Filter (LVF) for the VISNIR and bandpass filter at short wavelengths bonded to a narrowband LVF at long wavelengths for the IR] using slowly varying signal levels across the detectors. After integrating the filters, their alignment (which is particularly critical for the narrowband LVF of the IR FPA) was verified with the same setup.

The major steps of detector characterization relevant for radiometric calibration are as follows:

1. Validation of the MAJIS specific readout procedures at 100 kHz and 1 MHz,[13] which had been defined using a "reject grade" FPA. It was important to verify that a near-optimal performance was also obtained with flight FPAs over the full operating range of MAJIS in terms of detector temperature and integration time.
2. Characterization of the non-linear behavior with the increasing signal of the operable pixels of the flight VISNIR and IR detectors, so as to be able to derive a linearity corrected DN level from the actual DN level.
3. Determination of the conversion efficiency (e^-/DN) and readout noise for the VISNIR and IR flight detectors in the low signal range with 100 kHz and 1 MHz readouts. Applying the conversion efficiency relevant to the readout being implemented to the linearity corrected DN levels then provides a reliable evaluation of the actual number of collected e^- for each operable H1RG pixel.
4. Evaluation of the operability for the VISNIR and IR flight detectors, i.e., the percentage of usable pixels excluding dead pixels, hot pixels, and unreliable pixels, for sets of operating conditions (FPA temperature and integration time) relevant for MAJIS science investigations.
5. Evaluation of the persistence between successive acquisitions so as to validate the on-board de-spiking procedure of MAJIS.

The results of these measurements are presented in Sec. II.

The next step was performed as part of the calibration of the integrated MAJIS instrument (Sec. III). Sources with known radiances (black bodies whenever possible) were used for determining the instrument transfer function (ITF) of the VISNIR and IR channels, i.e., the electron collection rate obtained with a radiance of 1 $W/\mu m/m^2/str$ for every wavelength and location in the FOV. When combined with the conversion efficiency (e^-/DN) determined during characterization, this makes it possible to convert MAJIS DNs into radiances for each data element. The ITF is a complex combination of the following factors:

- Optical efficiency of the telescope for each pixel location in the FOV and wavelength.
- Transmission coefficient (IR) or reflection coefficient (VISNIR) of the beam splitter as a function of wavelength.
- Dispersion efficiency of the grating for each pixel location in the FOV and wavelength.
- Transmission of the filters integrated close to the FPA for order sorting for both FPAs and for thermal background reduction for the IR FPA.
- Quantum efficiency as a function of wavelength (this conversion factor from photons to electrons is always lower than 1).

Nominal sampling for MAJIS science observations is obtained by averaging the 18 μm H1RG pixels by 2 in both the spectral and spatial directions so that the FOV corresponds to 400 MAJIS pixels (36 μm pitch) and the spectral range of each channel corresponds to 508 MAJIS nominal spectels (see Fig. 1). However, it is possible to select by TC oversampled spectral ranges covering up to 132 nominal spectels. In these ranges, the signal from the detector is not averaged by 2 in the spectral direction so that up to 640 wavelengths can be sampled. As there is full flexibility for selecting oversampled spectral ranges, a reliable radiometric calibration is required for 1016 oversampled spectels in both the VISNIR and IR spectral ranges. Furthermore, the first row of each channel can be selected by TC so as to obtain the best possible match between the VISNIR and IR FOV. This offset can be odd or even, and it may have to be modified after launch or depending on the thermal environment (if the

two channels have slightly different thermo-elastic characteristics). Therefore, similarly to the characterization of the detector, the radiometric calibration of the integrated instrument was performed in the FOV at the 18 μm level (800 × 1016 connected H1RG pixels).

With the MAJIS HxRG readout procedure,[13] dark current subtraction is required for achieving accuracy even for very small signal levels (a few e^-). The on-ground data processing pipeline will have access to the configuration TC setting up each observation; hence, it will be able to derive the radiance of a given data element from its linearity corrected DN level after subtraction of a dark current (considering possible FPA temperature evolutions during an observation) by averaging the conversion factors corresponding to the actual H1RG pixels contributing to this data element. If a non-operable H1RG pixel is included, the data element will be flagged as non-operable.

The radiometric measurements revealed that with QTH or blackbody sources, there is a significant stray light contribution for the VISNIR channel at short wavelengths (490–1200 nm) and at the upper end of the VISNIR wavelength range (2250–2350 nm). This VISNIR stray light does not exhibit strong spectral features except in a narrow spectral range (600–700 nm) so that it has only a limited impact on the identification of legitimate spectral features, which will be observed at the same spectral location but with a lower contrast due to stray light. The radiometric calibration of the VISNIR channel as presented in Sec. III aimed at evaluating the instrument response for the legitimate contribution.

II. RESULTS OF THE DETECTOR CHARACTERIZATION CAMPAIGNS RELEVANT FOR RADIOMETRIC CALIBRATION

A. Instrumental setups for characterization

As indicated in Sec. I, the characterization of the FM VISNIR detector has been performed at IASB Brussels (Belgium) and that of the FM IR detector has been performed at IAS Orsay (France). In the configuration used for the characterization of the performance of the IR detector, it was shielded from incoming light by a cover, which could be controlled from 90 K (dark current) up to 115, 120, and 135 K (linearity with time). The operating temperature of the detector was controlled by a cold finger for the two characterization setups over a range covering with margins expected for science investigations, including the nominal operating temperature. The detector characterization temperatures are presented in Table I.

B. Validation of the MAJIS readout procedures with flight detectors

During characterization, the digital frames coming out of the FPE (16 bits with 100 kHz readout and 12 bits with 1 MHz readout) were acquired using the test setup provided by Teledyne. A single gain setting of the FPE was selected with both readout modes for characterization and calibration observations as the digital range with this gain adequately covers the analog ranges of the IR and VISNIR flight detectors.

The first results obtained with flight detectors using the MAJIS specific H1RG readout procedures have been presented in Ref. 13. These validations over the full dynamic range of interest for MAJIS science observations are of primary interest for MAJIS radiometry as they demonstrate how MAJIS will meet specifications for radiometry from very low signal levels (down to 10 e^-) to near saturation.

As indicated in the Introduction, MAJIS uses CDS readout procedures for both 100 kHz and 1 MHz readouts. With an HxRG, a second step of processing, "row correction" (rows corresponding to the spectral direction), is performed so as to obtain consistency between successive acquisitions by the same row. It subtracts an average of the signal level for the eight reference pixels at the beginning and end of each row, which constitute a reference for a signal level of 0 as they are not connected to the sensitive layer.

As shown in Fig. 2 (top panel), the dispersion between frames much exceeds the noise level, which would be a major issue for the precision of low signal levels and for de-spiking, which relies on a series of acquisitions of a scene. After subtracting the average reference pixel level from the signal levels on the same row, the residuals of each acquisition compared to the average of the 24 acquisitions (Fig. 2, bottom panel) are in line with the noise model, which will be presented in Sec. II C. Therefore, bias correction along columns, a standard procedure for HxRG detectors, achieves precision as series

TABLE I. Operating temperatures for the characterization of the VISNIR and IR FM detectors.

	Nominal (K)	Other test temperatures (K)
VISNIR	132	125, 145
IR	90	75, 80, 85, 95, 100, 105

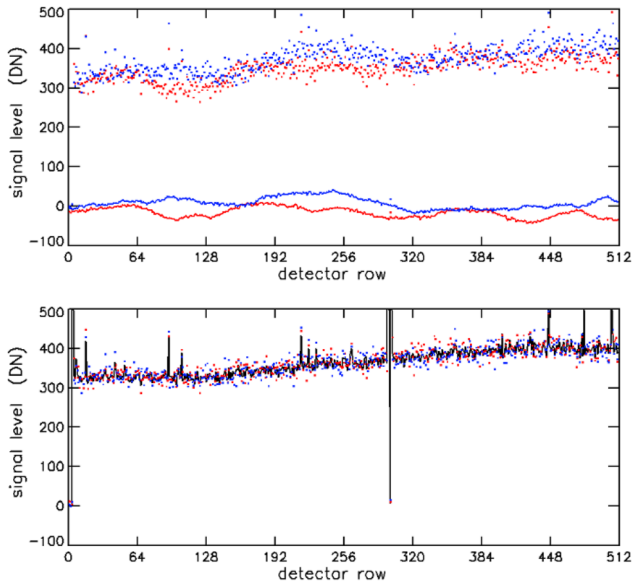

FIG. 2. Top panel: Signal levels (blue and red dots) along one column of the IR FM detector readout at 100 kHz for two acquisitions of a constant signal out of a series of 24 acquisitions. The blue and red solid lines correspond to the average of the two frames of the eight reference pixels on each detector row. Bottom panel: Signals from the two frames after row correction (blue and red dots) compared to the average of the 24 frames (black line).

of acquisitions are consistent within the limits of the total expected noise.

The next requirement is to achieve accuracy. This is also not straightforward with the H1RG. As shown in Fig. 3, there are biases along the rows, which are specific to each of the 16 readout channels.

As will be shown in Sec. II C, each DN corresponds to slightly more than two e^- with 100 kHz readout so that the biases in Fig. 3 would drastically impact measurements of weak signals. With 100 kHz readout, the similarity between the biases at the bottom and top of the detector makes it possible to use the eight reference lines for correcting the biases. This approach is not available to MAJIS for two reasons: First, the FOV of MAJIS extends over 800 rows near the center of the 1016 rows with connected pixels. Reading out the full detector at 100 kHz would increase the readout time, which would decrease the time available for signal acquisition. More importantly, a different pattern of biases is observed with the 1 MHz readout mode, which will be used for more than 85% of MAJIS science acquisitions.[1]

With 1 MHz readout, each DN corresponds to ~32 e^-; hence, the biases along a row are also quite significant for low signals (see Fig. 4). The bias levels, which are larger at the bottom row, increase across each channel. Due to the very different behavior of the bottom and top reference rows, one cannot legitimately use them for correcting the 1016 intermediate rows.

Therefore, for science observations, MAJIS implements a channel bias mitigation approach which does not rely on reference lines. It consists in subtracting a dark signal obtained with the shutter closed from the signal obtained with the shutter open. Dark signal subtraction was anyway required for the IR channel: before integration, the dark signal is constituted primarily by the dark current, which exceeds 1000 e^-/s for temperatures higher than 95 K. After integration, the thermal background from the spectrometer can reach even higher levels at long wavelengths.

As shown in Fig. 5, dark subtraction very effectively corrects conversion channel biases. It also much improves the cosmetics even under poor operability conditions, as this observation was performed at 95 K with an integration time of 800 ms (see Sec. II E):

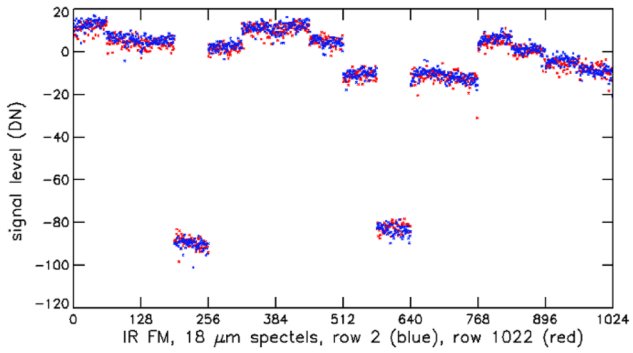

FIG. 3. Signal levels averaged over 24 acquisitions with 100 kHz readout of the IR FM detector for two of the eight reference rows: row 2 (blue, near the bottom edge of the detector) and row 1022 (red, near the top edge of the detector. Major steps are observed from one of the 16 readout channels to the next, with smaller variations within each channel. The bottom rows (blue) and top rows (red) behave quite similarly.

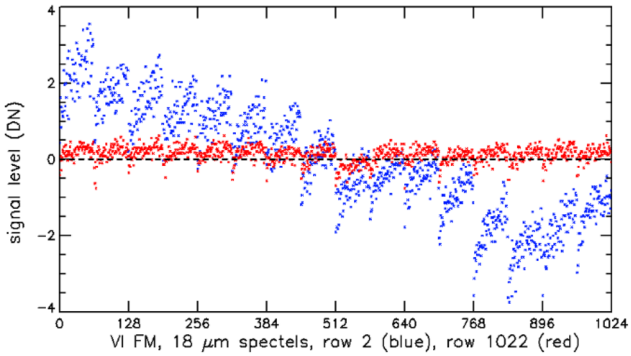

FIG. 4. Biases averaged over 32 VISNIR acquisitions with 1 MHz readout along two reference rows, one near the bottom edge of the detector (blue) and the other near the top edge of the detector (red).

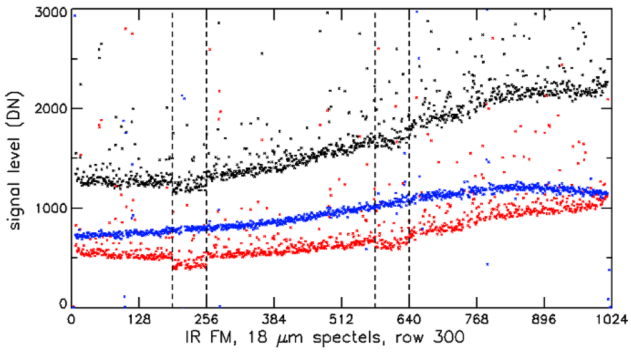

FIG. 5. IR FM signal obtained with 100 kHz readout for a temperature of 95 K and an integration time of 800 ms (black) averaged over 24 frames; "dark" signal with the source off (red) averaged over 24 frames; dark subtracted signal (blue). The dashed lines correspond to the two readout channels (4 and 9) with lower signals for reference lines (see Fig. 2).

dark subtraction results in a very smooth profile of the signal, with most "warm" pixels (with a higher dark current than the median) back in the fold after dark subtraction. The dark subtraction approach cannot be applied to the dark signal itself. Therefore, the IR dark signal will be evaluated in flight during calibration sequences with 100 kHz readout of the full detector so that the reference line approach can be implemented for tackling biases along rows.

For the VISNIR channel, both the dark current and the thermal background (after integration) are very small; hence, dark subtraction was at first considered as optional. However, the channel biases are very stable within the same operating conditions, and subtracting a dark current very effectively removes the biases along rows with both 100 kHz readout and 1 MHz readout as shown in Fig. 6 (same dynamic range as Fig. 4).

Acquiring and then subtracting a VISNIR dark signal is not penalizing for MAJIS science operations, as it can be acquired at the same time as the IR dark signal (most observations will be performed with both channels). The impact on the signal-to-noise ratio (SNR) is very small as dark signals are determined from a series of nine acquisitions with the shutter closed and the same parameters as the

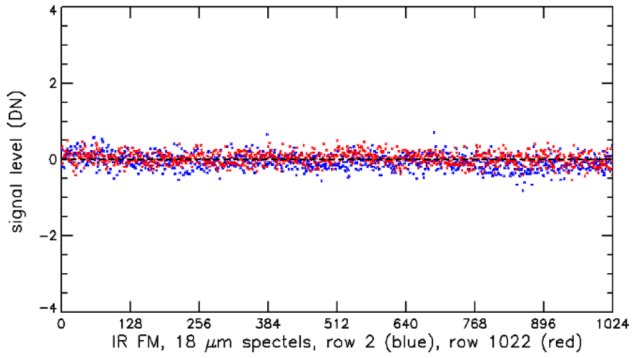

FIG. 6. Dark subtracted signals averaged over 24 acquisitions at 1 MHz for row 2 (blue) and row 1022 (red) of the VISNIR FM detector.

actual observation. Therefore, the impact on SNR is at most a factor sqrt(1 + 1/9), i.e., 1.055, in the readout noise dominated signal range, and it becomes negligible as soon as the shot noise becomes dominant. This is a small price to pay for achieving both precision and accuracy within the limits of the noise model of the VISNIR channel (see Sec. II C).

Once the 1 MHz and 100 kHz readout procedures had been validated, it became possible to compare dark subtracted series of frames obtained with both readout modes for the same signal level. The results show a very consistent ratio (~15.54) between the DN levels for low signals as shown in Fig. 7.

No discrepancy has been observed down to very low signal levels within the limits of the noise models for both readout modes (the 1 MHz readout mode has a higher readout noise than the 100 kHz readout mode, see Sec. II C). As can be seen from Fig. 7, the inter-pixel variability of operable pixels for the IR detector is low (~1.4%), resulting in smooth profiles of the raw data for sources with little high frequency variability. The inter-pixel variability of the VISNIR detector is even lower (~0.7%).

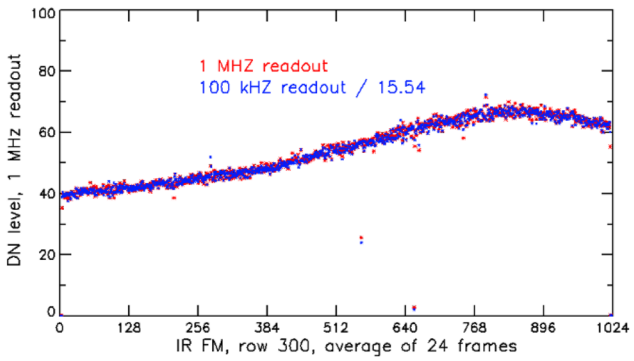

FIG. 7. Signal profiles along a row of the IR FM detector averaged over 24 frames with dark subtraction. The same signal was observed with 100 kHz readout (blue) and 1 MHz readout (red) with an integration time of 800 ms.

C. Characterization of the non-linear behavior of the VISNIR and IR MAJIS detectors

The analog-to-digital conversion (ADC) by the FPE of the output signal from the detector is expected to be close to linear in terms of DN/μV. However, HxRG detectors exhibit a decrease in transimpedance (μV/e$^-$) as a function of the signal level, which is well documented.[9,10] This means that the number of electrons required for reaching a given signal level in DNs increases faster than the signal level itself. As the detection chain is non-linear, before applying the same conversion coefficient to a given spatial and spectral data element whatever the signal level in DNs, one therefore must convert the raw DNs into DNs corrected for linearity.

The transimpedance is expected to decrease linearly with the output voltage, itself proportional to the signal in DNs. Therefore, one should have

$$DN_c = DN/(1 - A \times DN), \quad (1)$$

where DN_c is the DN level corrected for linearity and A is the slope of the relative decrease in transimpedance expressed in DNs instead of μV.

The integration time is the interval between the first and second CDS readouts, which can be selected by steps of 1 ms by command to the FPE. This makes it possible to compare the DN levels corresponding to a constant signal over a wide range of integration times. The best fit for the "slope" coefficient is that for which the DN increase rates after applying dark subtraction align for all integration times to that of a reference integration time until levels close to saturation are reached. 24–32 acquisitions are averaged for each integration time so as to obtain a very high SNR. This approach was very successful for the IR FM detector.

As shown in Fig. 8(a), the linearity of the IR FM detector at 85 K can be modeled with a decrease in the transimpedance of 4×10^{-6}/DN with 100 kHz readout (a factor of 15.54 has to be applied to DNs with 1 MHz readout as shown in Sec. II B). This applies to all operable pixels (see Sec. II E) within 1.5% over nearly the full dynamic range. The same coefficient applies to DN levels at other operating temperatures of the IR detector up to the limit of operability for both the 1 MHz and 100 kHz readout modes, as shown in Figs. 8(c) and 8(d). These results make it possible to apply the same linearity correction coefficient to all IR data whatever the temperature of the FPA.

This approach also obtained good results with the VISNIR detector, as shown in Fig. 8(b). For this detector, the coefficient to be applied for obtaining linearity corrected DNs using Eq. (1) is smaller (1.85×10^{-6}/DN for 100 kHz readout) and the fit is even better (within 1%) for low to medium-high signal levels than for the IR detector. However, contrary to the IR detector, the rate of increase of the signal begins to drop for signals ~10% lower than saturation so that the correction coefficient was adjusted in this range. This is not nominally relevant for science observations, as integration times will be selected so as to stay further away from saturation, but it will make it possible to recover usable data if the signal is larger than expected.

At this stage, detector characterization had achieved its main purpose for preparing radiometric calibration, as a procedure was identified for obtaining reliable linearity corrected DN levels, which

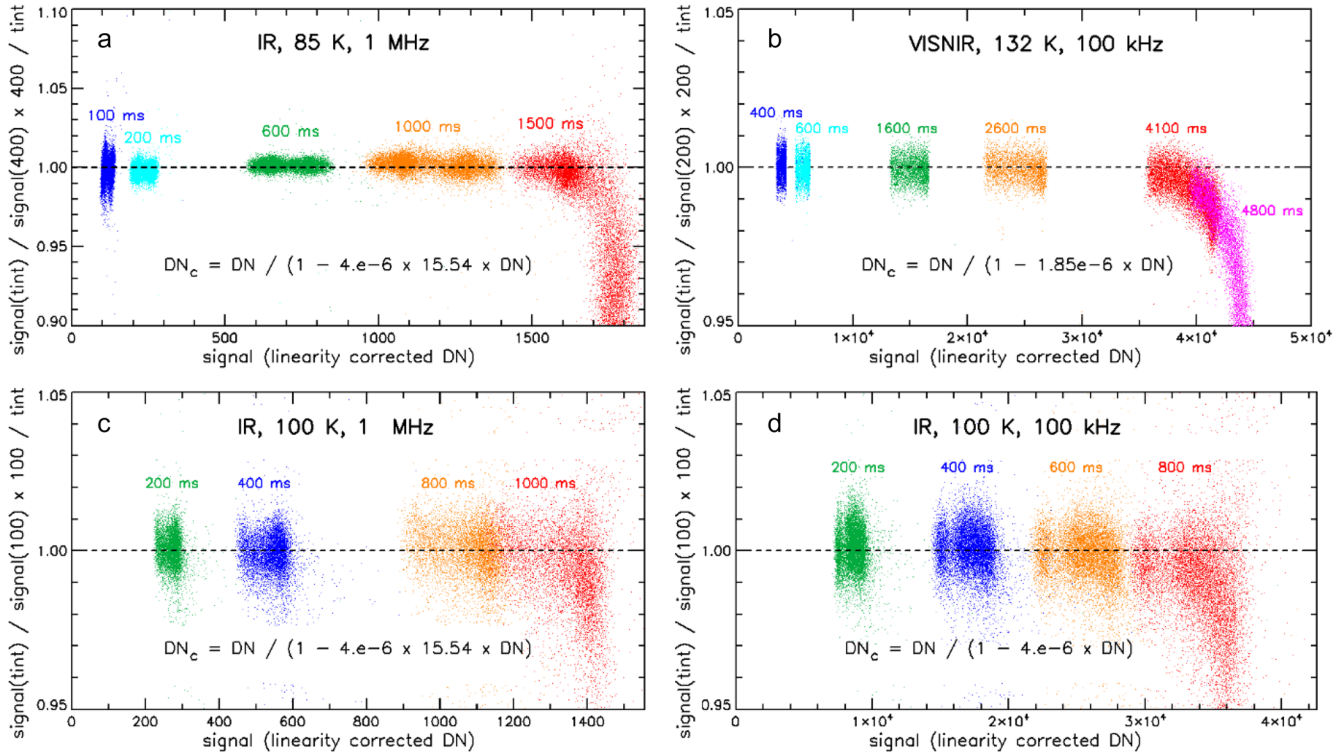

FIG. 8. Best fit assuming a linear decrease in the transimpedance for (a) the IR FM detector at 85 K with 1 MHz readout, (b) the VISNIR FM detector at 132 K with 100 kHz readout, (c) the IR FM detector at 100 K with 1 MHz readout, and (d) the IR FM detector at 100 K with 100 kHz readout. For each series, the signal corrected for linearity obtained with integration times leading to signals ranging from low levels to saturation is compared to that with a reference integration time [(a) 400 ms; (b) 200 ms; and (c) and (d) 100 ms].

could be compared to the signal from radiometrically calibrated sources.

D. Determination of the conversion efficiency (e^-/DN) and readout noise

The next step is to obtain information on the conversion efficiency (e^-/DN) and readout noise (e^-) over the full range of integration times and operating temperatures so as to compare them with MAJIS specifications, with the performance expected from a H1RG at 100 kHz, and with the results obtained by Teledyne at the nominal operating temperatures. This was particularly important for the 1 MHz readout mode, which is specific to MAJIS.

The standard procedure for evaluating the readout noise consists in building up a noise model combining the shot noise with the readout noise. For this purpose, two issues have to be considered: the non-linearity of the H1RG detector and an electrical crosstalk contribution, which has an impact on the contribution of the shot noise to the total noise.

The noise model must be elaborated using linearity corrected signal levels in DN, using the procedure presented in Sec. II B. One also needs linearity corrected signal levels in DN for the standard deviation. A deviation in either direction leads to an increment or decrement of the actual signal, which is reflected in DN levels as a function of the local slope of the conversion function so that the correction coefficient to be applied is the derivative of that in Eq. (1),

$$\mathrm{DN}_c(\,\mathrm{stdev}) = \mathrm{DN}(\,\mathrm{stdev})/(1 - \mathrm{A}\,\mathrm{DN}(\mathrm{signal}))^2, \qquad (2)$$

where "stdev" stands for standard deviation. The series of acquisitions with increasing integration times used for evaluating linearity provide a range of increasing shot noise, which adds quadratically to the readout noise. The outcome for 1 MHz readout of the IR detector at 75 K is shown in Fig. 9. At this temperature, the dark current is very low (a few e^-/s) so that a dark acquisition provides a direct evaluation of the readout noise in DN (not yet in e^-).

As shown in Fig. 9, there is a large dispersion of standard deviations for pixels with similar signals, which makes it difficult to constrain the noise model. This is surprising as the shot noise should be nearly the same and the readout noise should also be the same for neighbor data elements being read out by the same conversion channel. This dispersion is due to the number of acquisitions (24), which is too low by itself for obtaining an accurate determination of the standard deviation. This is demonstrated by Monte Carlo simulations with 100 000 sets of 24 samplings around 0 with a pre-defined standard deviation. The distribution of standard deviations evaluated for each set of 24 simulated values fits very well the distribution

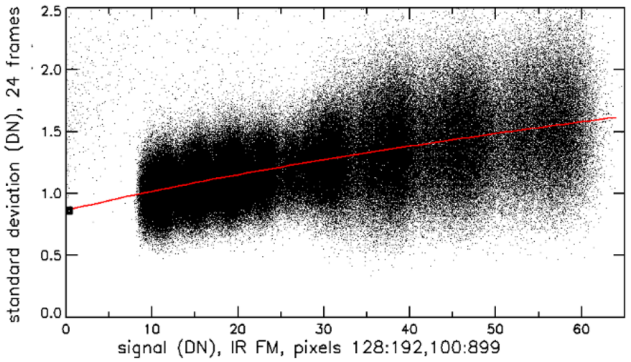

FIG. 9. Linearity corrected signal and standard deviation among 24 acquisitions for 41 000 pixels from channel 2 (columns 128–191) at nine integration times with a weak source. The black square on the Y axis is the readout noise in DN as determined from a series of dark acquisitions. The red line is a first attempt at a noise model fitting the data.

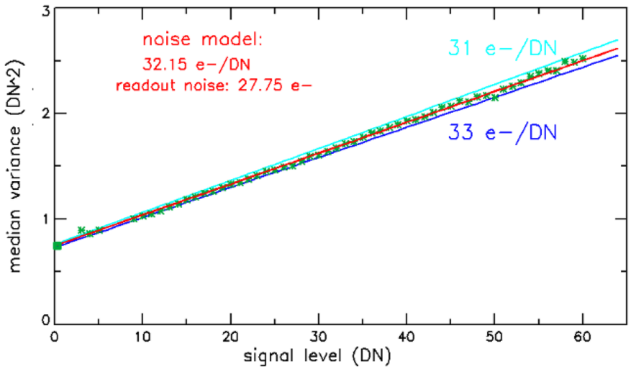

FIG. 11. The green stars correspond to variances (in DN^2) evaluated as discussed in the text (a few additional data points have been added using a shorter integration time). The green square corresponds to the variance for the dark current (no signal). The red line is the best fit noise model. The light blue and dark blue lines indicate the upper limit (33 e^-/DN) and lower limit (31 e^-/DN) at 3 σ of the conversion efficiency compatible with the data.

of standard deviations of actual series of 24 measurements for pixels selected on the basis of signal level (Fig. 10).

The simulations show that the dataset is consistent as expected with a single standard deviation for all pixels in each of the two sets. This makes it possible to accurately evaluate the standard deviation (hence the variance) by comparing the median value of the dispersions with that for a Monte Carlo simulation of a standard deviation of 1 DN and the same number of samples (24). This can be done with all populated bins 1 DN wide. As shown in Fig. 11, with this procedure, the data points for the variance as a function of signal fit very closely a straight line, as expected for a noise model combining readout noise and shot noise.

The last step is in part model dependent, due to a specific feature of many array detectors, including HxRGs, which was identified as quantum efficiencies (e^-/photons) determined from noise models[12] turned out to be larger than 1. Part of the output when reading out a pixel is contributed by the four neighbor pixels. As these four

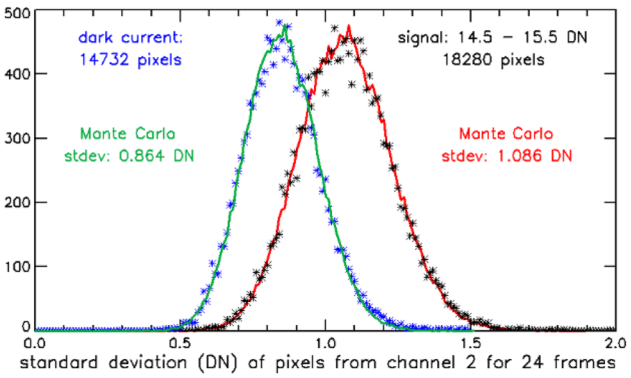

FIG. 10. Histogram of standard deviations for the 18 280 pixels with signal levels from 14.5 to 15.5 DN in Fig. 11 (black) and for 14 732 pixels also from channel 2 with dark current (blue). The red and green curves correspond to a Monte Carlo simulation of the same numbers of series of 24 samplings with standard deviations of 1.086 DN and 0.864 DN.

contributions are uncorrelated with the central one, this reduces the apparent shot noise. The resulting coefficient [Inter-Pixel Capacitance (IPC)] cannot exceed 1, and it is larger than 0.8 for most array detectors. The IPC acts as a multiplying factor in a noise model for both the conversion efficiency and the readout noise. With an IPC of 0.93 (in the range recommended by Teledyne), the best fit in Fig. 11 leads to a conversion efficiency ~32.15 e^- and a readout noise ~27.75 e^-, which far exceeds MAJIS requirements (readout noise < 80 e^- for short integration times requiring 1 MHz readout). The selected IPC could be off by a few percents, which would have a minor impact on the conversion efficiency and the readout noise. However, this would not impact the radiometric calibration results relevant for the MAJIS data pipeline (DN/unit of radiance for each MAJIS data element) as they are obtained by directly comparing the MAJIS data in DNs (after linearity correction and then dark subtraction) with the radiances of calibrated sources (see Sec. III).

The same approach has been used for all channels with 1 MHz and 100 kHz readouts for both the IR detector[16] and the VISNIR detector[17] at different temperatures.

The results show that the conversion efficiency is similar for the 16 channels with both 1 MHz and 100 kHz readouts over the full operational range. The readout noise over the full operational range is also similar to that at 75 K. There is, however, a significant increase in the readout noise for channels to the right of the IR detector (see Fig. 12), which seems to result from the characterization setup as this trend was not observed either during calibration of the integrated instrument or during the first tests after launch. For the IR detector, the readout noise at 100 kHz (~13 e^- for the left channels[16]) is well within MAJIS specifications: 20 e^- for very weak signals requiring long integration times for which 100 kHz readout is appropriate. The readout noise and conversion efficiency of the IR detector only marginally increase with the operating temperature.[16] For the VISNIR detector,[17] the readout noise at 1 MHz is slightly above 34 e^- (well within specifications), while the readout noise at 100 kHz is ~20.5 e^-. The readout noise at 100 kHz is marginal with respect to MAJIS requirements for long integration times (< 20 e^-),

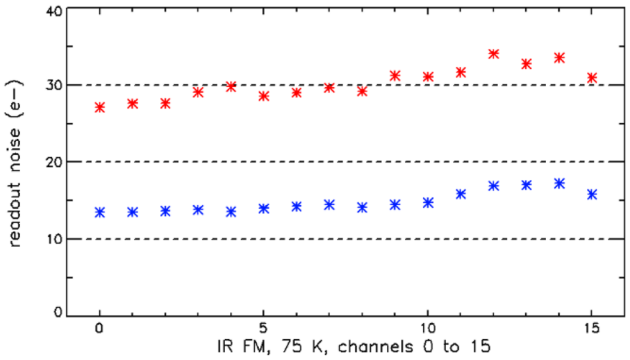

FIG. 12. Readout noise at 1 MHz (red) and 100 kHz (blue) for the 16 channels of the IR detector at 75 K, assuming an IPC of 0.93.

but this is more than compensated by a larger than expected well depth (~100 000 e^- compared to a specification of 60 000 e^-), which makes it possible to use longer integration times, improving the SNR. Table II summarizes the characterization results for conversion efficiency and readout noise. The readout noise levels of the left channels have been selected as representative of those observed with the integrated instrument.

During the calibration of the integrated instrument, the frames sent by the FPE were processed by the MAJIS proximity electronics (PE) as a first step in generating MAJIS data (see Ref. 1). With 100 kHz readout, the two frames acquired for CDS are issued as 16 bits unsigned DNs by the FPE. The PE divides the result of the CDS subtraction by 2, storing the post-CDS DN levels as 16 bit signed integers in its RAM. Therefore, the MAJIS DN (DN_M) at 100 kHz corresponds to twice more electrons than the values in Table II. With 1 MHz readout, the two frames acquired for CDS are issued as 12 bit unsigned DNs by the FPE. The PE multiplies the result of the CDS subtraction by 8 so as to store the signal levels with the same digital dynamics (16 bit signed integers) as 100 kHz data. The 16 bit signed dynamics is maintained in further processing steps by the main electronics of MAJIS by averaging instead of binning. As a result, the MAJIS DNs at 1 MHz correspond to eight time less electrons than the values in Table II, leading to similar values for 100 kHz and 1 MHz (VISNIR: 4.32 and 4.196 e^-/DN_M; IR: 4.26 and 4.1375 e^-/DN_M). These factors were considered when correcting MAJIS DNs for linearity. With this approach, the quantization noise (0.289 DN, ~1.2 e^-) is negligible with both 100 kHz and 1 MHz readouts when the PE performs row correction by subtracting the average of 8 reference pixel values from the data. It can have an impact for weak signals with high levels of on-board spectral, spatial, or frame averaging, which reduce the physical noise while retaining the same quantization noise.

E. Operability

Operability is defined by the proportion of usable pixels, excluding the pixels with a signal level much higher than that of their neighbors ("hot pixels," up to saturation), the pixels with a very low signal level ("dead pixels"), and the pixels for which the dispersion between successive values is higher by a factor of 2 or more than that expected from the noise model ("unreliable pixels"). The data obtained with the same integration time for the 100 kHz readout mode and 1 MHz readout mode are always consistent within noise limitations after applying the 15.54 gain ratio to 1 MHz data except when close to the saturation level, which is higher at 1 MHz than at 100 kHz.[16,17] Therefore, the only relevant parameters controlling the operability are the integration time and the temperature of the detector.

In this respect, the situation is drastically different for the VISNIR detector and the IR detector. For the VISNIR detector, there is no indication that electrons can move from one pixel to the next in the sensitive layer during the integration time. Even with incoming fluxes close to saturation, the signal for columns 4 and 1019, next to unconnected reference columns, closely matches that for columns 5 and 1018, which would not be the case if electrons generated in the neighbor unconnected columns, which cannot be collected by the underlying diodes, could move across pixel boundaries. Furthermore, the dark current is very low so that its increase with temperature has no impact. As shown in Table III, the operability is very high, in the 99.7% range for 18 × 18 μm^2 pixels, with very little dependence on the integration time and the operating temperature. For nominal science operations, MAJIS implements 2 × 2 averaging (1 × 2 averaging with spectral oversampling, see Ref. 1). In a conservative approach, an averaged data element is considered as not operable if any of its component is not operable. As most un-operable 18 μm pixels of the VISNIR detector are isolated, the operability after 2 × 2 averaging is ~99%, which far exceeds the MAJIS specification for operability (95%).

The IR detector behaves quite differently: the number of 18 μm hot pixels is in the same range of that of the VISNIR detector (2500) only for the lower end of the operational range of temperatures (85–97 K) and integration times (70–800 ms). For these hot pixels, the dark current is higher than that of operable pixels by factors that can exceed 100. The dark current increases by a factor of 4 for every 5 K increase in temperature[16] (a factor of 64 from 85 to 100 K) so that

TABLE II. Conversion efficiency and readout noise for the VISNIR detector and the IR flight detector at its nominal operating temperature (90 K).

	Conv. eff. (e−/DN)	Readout noise (e−)
VISNIR, 100 kHz	2.16	20.5
VISNIR, 1 MHz	33.57	35
IR, 100 kHz	2.13	13
IR, 1 MHz	33.1	30

TABLE III. Operability of 18 μm pixels of the VISNIR FM detector with nominal integration times: 800 ms for 100 kHz readout and 100 ms for 1 MHz readout.[17]

Temp. (K)	Integration time (ms)	Operability (%)
125	100	99.74
125	800	99.66
132	100	99.72
132	800	99.69

the number of isolated hot pixels increases both with temperature and integration time.

Another important element is that electrons collected in the sensitive layer of the IR detector can move to neighbor pixels as soon as the underlying capacitance is full (due to saturation) or if it is not connected to the sensitive layer (reference columns). Next to reference columns, these "spillover" electrons fill up each successive column up to saturation. An isolated hot pixel can reach levels close to saturation even for the acquisition immediately after reset, in which case its signal level is close to 0 after CDS. After integration, such a hot pixel generates large numbers of electrons, which spill over first to its four neighbors and then further away as the integration time or the detector temperature increases. A spillover contribution has a much higher noise than a legitimate signal so that any pixel next to a saturated pixel must be considered as non-operable. The impact of spillover electrons increases with integration time and detector temperature.

Before assessing the consequences on the operability of the IR detector, it is important to consider the likely operational conditions for the science operations of MAJIS.[1] When JUICE is distant from Galilean satellites, the IR radiator observes empty space ("cold case"), with a temperature of ~85 K from thermal modeling. A first validation was obtained from post-launch monitoring of the temperature of the IR detector evolution, which stabilized at ~87 K. Further improvement can be expected when JUICE reaches Jupiter, as a 25 times smaller solar flux is likely to result in a colder spacecraft interface and a reduced thermal contribution from sunlit elements in the FOV of the MAJIS radiators. Long integrations (800 ms or more) will only be implemented in the "cold case." When the sunlit surface of a Galilean satellite occupies a significant part of the FOV of the radiator ("hot case"), the temperature is expected to reach 96 K (worst case, including margins) according to thermal models. When close to satellites, dwell time and de-spiking constraints will result in integration times ≤100 ms.[1]

We selected a test region of 64 × 64 pixels in size for evaluating the effect of the temperature and integration time on the operability. Figures 13(a) and 13(b) show that the operability is excellent in the cold case as even the hottest pixels only impact their four neighbors. However, with nominal spectral averaging by 2, one nominal wavelength bin (6.5 nm) is lost at both ends of the wavelength range as the columns next to the four reference columns (column 4 at short wavelengths and column 1019 at long wavelengths) are impacted by spillover dark current e^- from the reference columns. The loss in operability when increasing the integration time by a factor of 4 is similar to that resulting to a temperature increase by 5 K (Fig. 13(e): 95 K, 400 ms; Fig. 13(f): 100 K, 100 ms). This trend shows that the dark current of hot pixels, while much larger than that of operable pixels, follows a similar dependence on temperature.

The characterization has been performed at intervals of 5 K. A temperature of 95 K and an integration time of 200 ms has been selected as representative of the operability at the upper limit of the modeled "hot case" (96 K, 100 ms). As shown in Fig. 13(c), column 4 is saturated by its dark current and spillover from reference columns. Figure 13(d) shows the impact of a signal of 5000 e^-, which is the maximum signal expected in 100 ms for "hot case" observations. Column 5 is now visibly impacted (and very noisy) due to the photoelectric electrons, which add up to the dark current in columns 0–4. However, even with the maximum expected signal, the impact

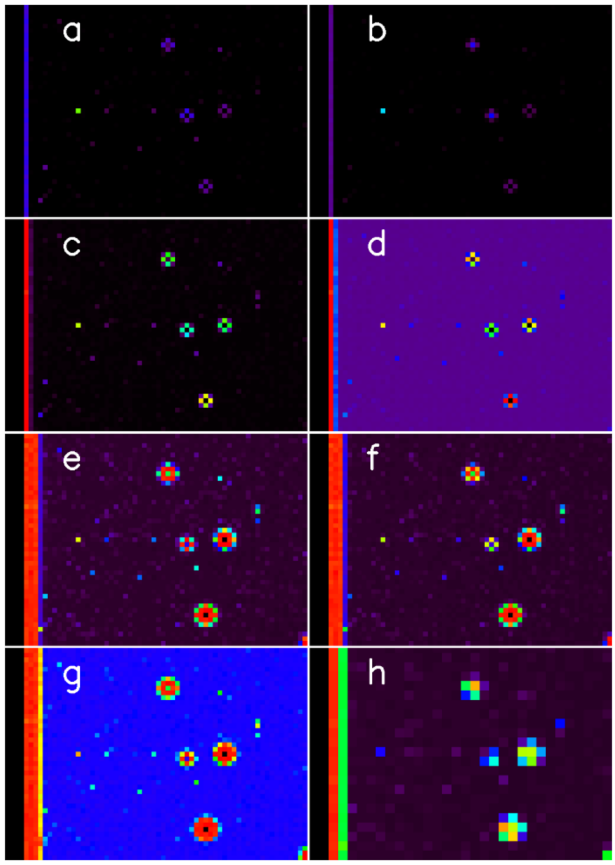

FIG. 13. Columns 0–63 of rows 624–668 for different IR detector temperatures and integration times. The "rainbow" color scale ranges from 0 (black, reference columns 0–3 on the left) to saturation (red); (a) no signal, 85 K, t_{int} = 800 ms; (b) no signal, 90 K, t_{int} = 100 ms; (c) no signal, 95 K, t_{int} = 200 ms; (d) 5000 e^- signal, 95 K, t_{int} = 200 ms; (e) no signal, 100 K, t_{int} = 400 ms; (f) no signal, 105 K, t_{int} = 100 ms; (g) 6000 e^- signal, 100 K t_{int} = 400 ms; and (h) same as (f) but with averaging 2 × 2.

of spillover on operability is still limited to the four neighbors of isolated hot pixels as in the cold case, and with nominal spectral averaging, the operable spectral range (506 wavelength bins out of 508, 2278–5561 nm) is the same as in the cold case.

The impact of a legitimate signal gets even more significant at high temperatures as can be seen in Fig. 13(g), where a signal of ~6000 e^-/pixel adds up to the dark signal displayed in Fig. 13(e) (100 K, 400 ms). The non-operable spectral range is now 4 pixels wide (two nominal wavelength bins), and as part of the well of pixels close to a hot pixel is occupied by a legitimate signal, spillover electrons have to spread further out, expanding the size of the non-operable clusters. Operability therefore depends on the signal level at high temperatures; hence, the operability evaluations in Table IV for integration times of 100 ms have been made with a signal level ~5000 e^- selected as representative of hot case observations.

At 80 K, the operability with 2 × 2 averaging (98.59%) is close to the value of 98.72% expected with 100 − 99.57 = 0.43% of independent un-operable 18 μm pixels. At hotter detector temperatures, the

TABLE IV. Operability for the IR FM detector as a function of detector temperature and integration time for H1RG pixels (no averaging) and with nominal MAJIS sampling (averaging of 2 × 2 H1RG pixels[16]). Values in italics correspond to an operability out of specifications (>95% with 2 × 2 H1RG pixels).

			Operability (%)	
T (K)	Readout mode (MHz)	Int. time (ms)	H1RG pixels	MAJIS pixels
80	1	800	99.57	98.59
90	1	100	98.63	96.74
90	1	800	98.10	95.27
95	1	100	98.34	96.10
95	1	800	97.16	*93.74*
100	1	100	97.37	*94.79*
105	1	100	96.47	*93.01*

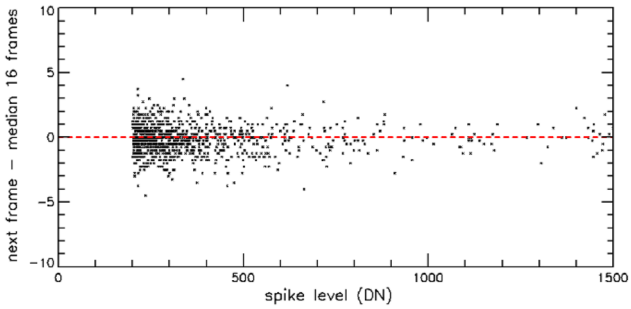

FIG. 14. Correlation plot between the level of a spike on a 18 μm pixel (up to 1500 DN, ~50 000 e^-, close to the full well) and the difference between the level of the next acquisition and the median of 16 frames in a series (excluding the spiked acquisition) acquired with 1 MHz readout and an integration time of 100 ms.

clustering of non-operable pixels much reduces the impact of nominal averaging on operability as shown in Fig. 13(f) (105 K 100 ms, no averaging) and Fig. 13(h) (105 K, 100 ms, averaging 2 × 2). With 100 − 96.47 = 3.53% independent non-operable pixels, 2 × 2 averaging would result in an operability of 86.6% instead of 93%. As a result, the operability requirement of MAJIS (95% with 2 × 2 averaging) is met up to a temperature of 100 K for the 100 ms integration times, which are relevant for "hot case" observations. Figure 13(f) (105 K, 100 ms, no averaging) shows that usable data can still be obtained even if the "hot case" modeling is off by 10 K.

In flight, operability will be monitored by observations at the 18 μm level with the shutter closed so as to identify additional hot pixels and with two sources in the internal calibration units. The operability maps will be updated accordingly, and additional criteria for declaring a pixel as non-operable will also be considered, in particular a contiguous saturated data element as one of the four neighbors.

F. Evaluation of the persistence between successive acquisitions with 1 MHz readout

A first series of tests on persistence had been performed on a "reject grade" IR detector. The results were positive for the 100 kHz readout mode as no anomalous signal was observed during the following acquisition for pixels hit by electrons with energies ranging from a few hundred kilo-electron volts to several mega-electron volts, which resulted in spurious signals ("spikes") reaching up to a major fraction of the full well.[18] Additional tests were performed at CSL Liège so as to confirm these results on a Teledyne engineering model for the IR EM detector (representative of MAJIS flight detectors). The main purpose was to test persistence with the 1 MHz readout mode specifically developed for MAJIS, which was not yet available during the first series of tests. This was particularly critical as 1 MHz readout is implemented for observations with short integration times, hence short intervals between frames.

As shown in Fig. 14, with the 1 MHz readout mode developed for MAJIS, the next acquisition after a spiked frame is in line with the other spike-free acquisitions with dispersion consistent with the 1 MHz noise model for the low signals of spike-free acquisitions. This validates the MAJIS de-spiking strategy[19] implemented on the fly by the MAJIS proximity electronics, which relies on splitting the integration time into short intervals and selecting the lowest values as those least likely to have been impacted by a spike.

III. RESULTS OF THE RADIOMETRIC CALIBRATION OF THE INTEGRATED MAJIS INSTRUMENT

A. MAJIS design elements and characteristics relevant for radiometric calibration and stray light issues

The design of the MAJIS instrument is presented in Ref. 1. After integration, photons collected by MAJIS go through a series of optical elements in the optical head before reaching the focal plane and the detector, each contributing to the overall optical efficiency as a function of wavelength.[20] Collected photons reach the spectrometers through a slit in the focal plane with a length of 14.4 mm corresponding to 800 pixels (18 μm pitch) and a width of 36 μm corresponding to the nominal spectral sampling (two pixels). This slit can be closed by a shutter so as to measure the dark current. A beam splitter then separates photons according to their wavelengths, photons with wavelengths lower than 2300 nm being reflected to the VISNIR spectrometer, while photons with longer wavelengths are transmitted to the IR spectrometer. The transmission and reflection efficiencies are presented in Fig. 15. As can be seen, the IR channel is very effectively protected by the beam splitter from low wavelength photons going through the slit, while up to 10% of photons with wavelengths larger than 2360 nm can enter the VISNIR channel.

After beam separation, the optical path for each channel goes through additional optical elements before reaching the VISNIR or IR detector, in particular the grating dispersing the photons along the spectral direction of the detector.[1] After dispersion, the FPA direction along the detector columns corresponds to the spatial direction along the slit (800 out of 1016 connected pixels). The direction along the detector rows corresponds to the spectral direction so that the 1016 connected pixels along the rows will be designated as "spectels" in the following. A filter is placed very close to each FPA so that its transmission as a function of wavelength is relevant for legitimate photons, high grating order photons, stray light photons, and thermal background photons. It has different characteristics for the IR and VISNIR channels. The IR filter[21] is designed

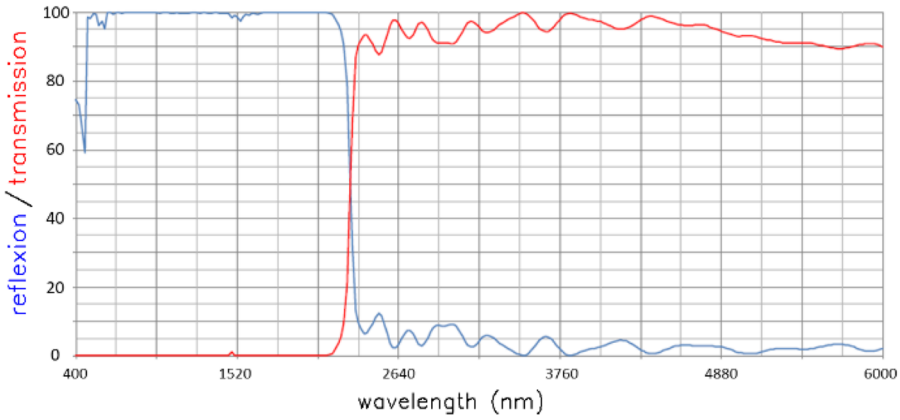

FIG. 15. Reflection (VISNIR) and transmission (IR) efficiencies of the MAJIS beam splitter.

for both rejecting high orders of the grating and the thermal background from the spectrometer, which provides large photon fluxes at wavelengths close to the upper spectral range of the IR channel (5565 nm). Therefore, it is constituted of a low pass filter covering the spectral range from 2270 to 2850 nm and a narrowband Linear Variable Filter (LVF) covering the spectral range from 2850 to 5565 nm. The FWHM of the LVF ranges from 4.25% to 3.6% of the central wavelength. Thermal background is not an issue for the VISNIR channel; hence, a high pass LVF was selected to perform order sorting by rejecting all photons with wavelengths shorter than ~70% of the nominal wavelength.

The different filter designs for the VISNIR and IR channels have a major impact on potential stray light issues, which are also impacted by the rejection efficiency of the beam splitter, which lets up to 10% of high wavelength photons reach the VISNIR channel (see Fig. 15). In the LVF spectral range of the IR channel (2850–5565 nm), only photons with wavelengths less than a few percentage away from the nominal wavelength can reach the FPA. For a given detecting element of the VISNIR channel, all photons with wavelengths larger than 70% of the wavelength corresponding to this element after dispersion and smaller than the cutoff wavelength of the VISNIR FPA (~2500 nm) can be effectively converted into electrons.

B. Radiometric calibration setup and procedures

The calibration setup at IAS Orsay[2] made it possible to control the temperature of the OH optical bench in the expected range for MAJIS science observations (125–140 K). The radiometric calibration of the IR channel was performed using a blackbody inside the calibration chamber and a single collimator mirror for illuminating the full FOV.[2] The blackbody emittance and collimator reflectance reduce the signal by a factor of ~0.97. During calibration, the temperature of the IR detector was controlled independently of that of the OH by a cold finger connected to the IR radiator.

The VISNIR detector is at the temperature of the OH optical bench with a small temperature increase during operations due to heating through the flex connecting the FPA to the FPE, which heats up to 160 K (100 kHz readout) or 170 K (1 MHz readout) for very long observations (1 h or more). Due to stray light issues, radiometric calibration of the VISNIR channel required combining observations with the internal blackbody illuminating the full FOV for long wavelengths, observations with an external blackbody with temperatures ranging from 250 to 500 °C covering a small part of the FOV, and observations of a QTH lamp illuminating an integrating sphere.

C. Radiometric calibration of the IR channel

1. Dark current evaluation

The radiometric calibration of the IR channel after integration was performed with the OH at two temperatures (126 and 137 K) representative of a "cold case" (far from icy moons) and a "hot case" (close to an icy moon), respectively.[2] The full range of radiometric characteristics was investigated when the IR FPA was stabilized at 88 K (cold case) and 96 K (hot case). The subsets of observations were performed with IR FPA temperatures ranging up to 100 K.[2]

As shown in Fig. 16, with an integration time of 800 ms, the dark signal can reach several 1000 e^- at short wavelengths (dark current) and levels close to saturation at long wavelengths due to the thermal background in the hot case. Therefore, for the IR channel, linearity correction must be performed on both the full signal (shutter open) and the dark signal (shutter closed) before dark signal subtraction to obtain accurate signal levels during radiometric calibration.

As discussed in Sec. III, the science acquisitions in the cold case will be performed with integration times ranging from less than 100 to 800 ms on the basis of saturation avoidance constraints for Jupiter hot spots and de-spiking constraints (longer integration times can be considered when far from Jupiter, with lower spike rates). The science acquisitions in the hot case (close to Europa, Ganymede, or Callisto) will be performed with integration times ranging from 64 ms (shortest integration time for the full FOV with 1 MHz readout) to 100 ms. In both cases, Fig. 17 shows that most of the dynamic range of the IR channel (larger with 1 MHz readout than with 100 kHz readout[16]) will be available for collecting photons.

The temperatures of the OH and FPAs are expected to be very stable in the cold case (far from icy moons). Subtracting a dark current determined from nine acquisitions before the observation will then provide accurate signal levels with a very minor impact

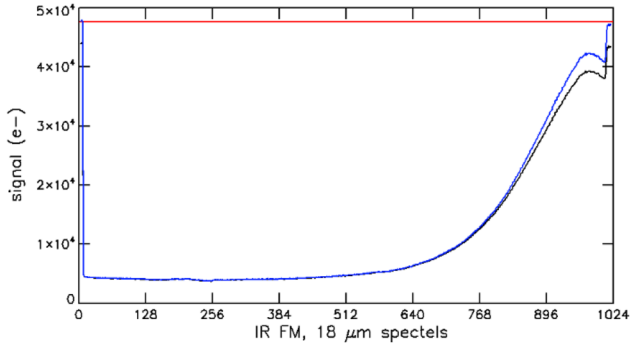

FIG. 16. Dark signal in the IR with the shutter closed for a FPA temperature of 100 K, 1 MHz readout, an integration time of 800 ms, and an OH temperature of 137 K. Black line: signal in e^- corresponding to raw DNs converted to electrons (4.26 e^-/DN for 1 MHz readout, see Sec. II D). Blue line: signal in e^- corresponding to linearity corrected DNs converted to electrons. Red line: saturation level (~48 000 e^- for 100 K, 1 MHz, 800 ms[16]). For each spectel, the median signal for pixels 300–500 has been selected to exclude non-operable pixels (see Sec. II E).

on SNR (see Sec. III) for most science observations. Most observations with very low signals (rings and exospheres) will be performed under "cold case" operational conditions. Attempting to detect signals down to a few e^- will require significant stacking combining frame, spatial, and spectral averaging. In most such cases, it will be possible to extend the observation to looking directions with no expected signal, providing an optimal reference for evaluating and correcting possible very low biases with the dark subtraction approach.

When close to Europa, Ganymede, or Callisto, the fraction of the FOV of the OH and IR radiators occupied by sunlit areas of the Moon will change with time so that the temperature of the IR FPA and OH may significantly vary. Dark signal measurements will then be needed before and after observations so as to model the dark current relevant for each frame by comparing FPA and OH temperatures at that time to that of the two bracketing dark signal measurements. Acquisitions performed with the shutter closed during radiometric calibration when the temperatures were evolving from one set of operating conditions to another showed that,

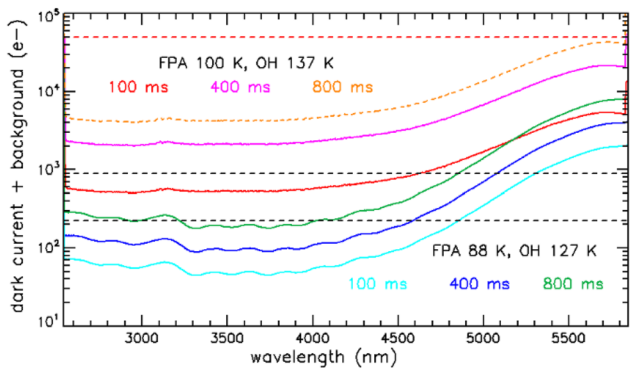

FIG. 17. Dark signal measured for a wide range of operation conditions during radiometric calibration.

even with temperature variations of several Kelvin, a linear interpolation performed in log scale (in which the dark current evolution is linear with temperature) provides a modeling of the dark current at intermediate temperatures with a bias 5–10 times smaller than the minimum noise (low signals). By applying these procedures, dark signal subtraction will not significantly impact the SNR in both the cold and hot cases.

2. Radiometric calibration dataset for the IR channel

The reference dataset for the radiometric calibration of the IR channel has been obtained with the FPA at 88 K and the OH at 126 K ("cold case"), 100 kHz readout and an integration time of 800 ms, which is the reference for 100 kHz readout.

The median radiometric performance across the FOV was derived from seven different temperature settings of the internal blackbody (+50, +30, +10, −10, −30, −50, and −80 °C). As shown in Fig. 18, the full wavelength range of the IR channel was covered with eight spectral ranges, selecting for each spectel a blackbody temperature for which the linearity corrected signal levels provided a high SNR while remaining well below saturation.

For spectels up to 700, the blackbody signal rapidly increases with wavelength (blue edge of the Planck function). Sixteen frames were averaged for each observation with the signal level from 5000 e^- to 32 000 e^- (see Fig. 18) so that the SNR ranged from 280 to 700. Additional data were obtained at shorter integration times (100, 200, and 400 ms) with 1 MHz readout. As discussed in Sec. II, the signals with both readout modes are very similar after correcting for the factor of 1.03 between the conversion efficiencies of the two readout modes in e^-/DN_M. Therefore, the radiometric performance is the same (within 1%) except for the last spectel of each of the 16 readout channels for which the signal is larger by a few percentage with 1 MHz readout for levels close to saturation.

The central part of the FOV was consistent with a flat signal as expected for the radiance from a blackbody. However, a near linear decrease in signal by up to ~17% was observed at the right side of the FOV (spectels 790–895) and a smaller decrease near the left edge (see Fig. 19).

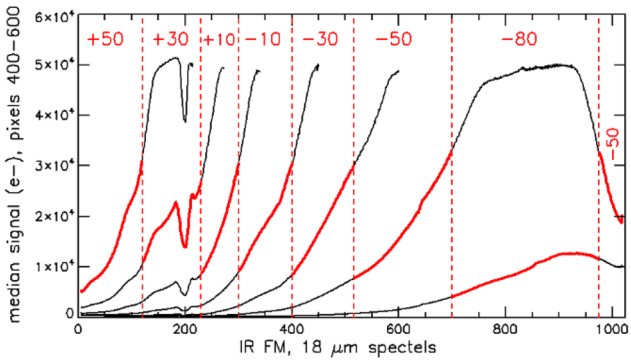

FIG. 18. Seven blackbody temperatures (°C) used for radiometric calibration in eight spectral ranges covering the 1016 connected spectels of the IR FPA (1014 not impacted by spillover from the reference columns in 800 ms at 88 K, see Sec. II E). The red lines indicate the blackbody temperature selected for each spectel.

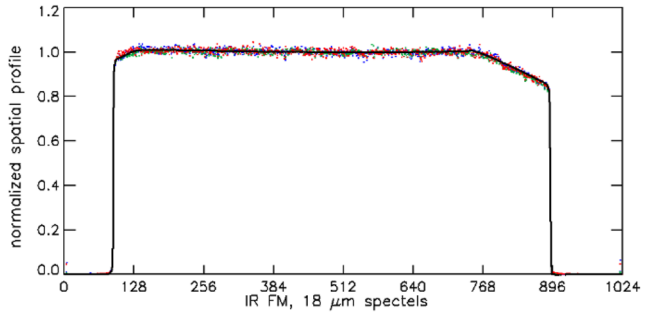

FIG. 19. Median signal along the MAJIS FOV with the blackbody at −80 °C for spectels 498–502 (3813–3830 nm, red dots), 648–652 (4310–4323 nm, green dots), and 798–802 (4813–4827 nm, blue dots) after normalizing for each spectel to the median of pixels 400–600, at the center of the FOV. A median of 5 spectels has been selected for minimizing the impact of hot pixels. The black line is the flat profile with minor vignetting at the left and right of the FOV, which was considered for radiometric calibration across the FOV.

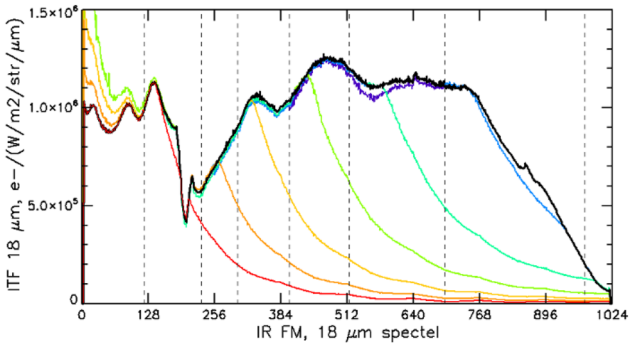

FIG. 20. Median ITF for pixels 500–520 (100 kHz readout, 800 ms, IR FPA at 88 K) obtained for each blackbody temperature by dividing the signal in e^- by the modeled radiance and the integration time. The results are consistent within a few percentage at domain boundaries. An interpolation with weights from 1 to 0 and 0 to 1 for the two relevant temperatures was applied across a range of 20 spectels so as to avoid small steps at domain boundaries when constructing the composite ITF (black line).

The spatial profile of all spectels in the LVF range is very similar, with linear decreases close to both edges of the FOV, most marked on the right side (see Fig. 19). Spatial profiles of other sources with an integrating sphere did not show these features; hence, the most likely interpretation is that the blackbody inside the vacuum chamber was slightly vignetted on both sides of the FOV due to the optical setup of the blackbody within the chamber. It was modeled by two linear slopes from a best fit of pixels 96-125 on the left side of the FOV and pixels 775–895 on the right side of the FOV.

3. 2D ITF for the IR channel

The instrument transfer function (ITF, e^-/unit of radiance, $W/m^2/\mu m/str$) could then be reconstructed for every pixel and spectel by dividing the signal in e^- by the radiance of the blackbody at the appropriate temperature for each spectel. A factor of 0.97 was applied combining the emissivity of the blackbody and the reflectance of the mirror. At the edges of the FOV, the vignetting as derived from Fig. 19 was applied to the radiance. This made it possible to obtain a two-dimensional ITF (800 × 1016) for all connected data elements in the FOV (800 × 18 μm pixel wide).

The results presented in Fig. 20 are very consistent when the signal is not saturated except at very short wavelengths. Another way of displaying the same data consists in comparing the radiance obtained from the ITF with the Planck radiance for each temperature multiplied by 0.97 (Fig. 21).

For each blackbody temperature, a perfect fit with the Planck radiance is a built-in feature for the spectral domain over which the ITF was evaluated on the basis of measurements with this blackbody temperature. However, except for significant residuals in the very short wavelength range (an issue that will be addressed in Sec. III A 4), the measured radiances in Fig. 21 are also in agreement with the expected radiance in other spectral domains, where the ITF was determined with the blackbody at a different temperature, as shown in Fig. 21 (bottom panel). This agreement extends over a dynamic range covering three orders of magnitudes, which shows that the linearity correction presented in Sec. III is adequate and that the measurements of very low signal levels are accurate.

This is confirmed in Fig. 22, which shows that the blue edge of the blackbody signal at −80 °C is reliably measured down to signal levels smaller than 40 e^- when applying an ITF determined from signal levels ranging from 10 000 e^- to 30 000 e^- with the blackbody at 30 or 50 °C (see Fig. 18). The standard deviation around the expected

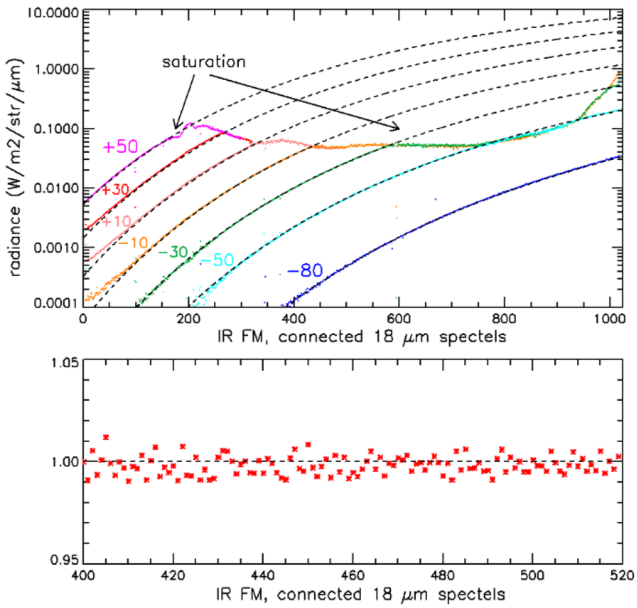

FIG. 21. Top panel: Radiances evaluated with the ITF (100 kHz) in the center of the FOV compared to the Planck radiances (×0.97) for each blackbody temperature (black dashed lines). Significant residuals are only observed for connected spectels 0–100. Bottom panel: Ratio of the radiance at the center of the FOV derived from an average of 16 frames and the ITF to the expected radiance with a blackbody temperature of −50 °C for a spectel range from 400 to 520 over which the ITF was determined at a temperature of −30 °C (see Fig. 18), with signal levels ~5 times larger than at −50 °C.

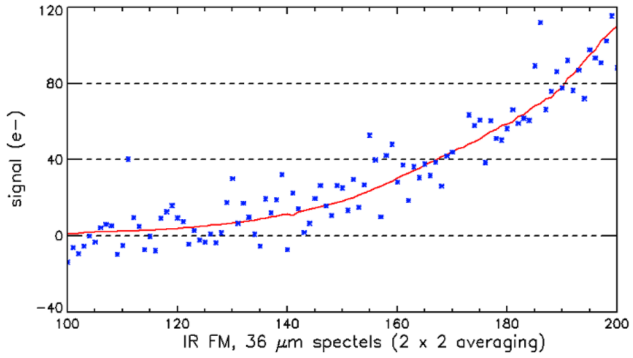

FIG. 22. Signal levels (blue dots) for one frame acquisition of a pixel in the center of the FOV evaluated with 2 × 2 averaging (nominal for science observations) with the blackbody at −80 °C. The red curve is the expected signal level from the ITF, the Planck radiance (×0.97) and the integration time (800 ms).

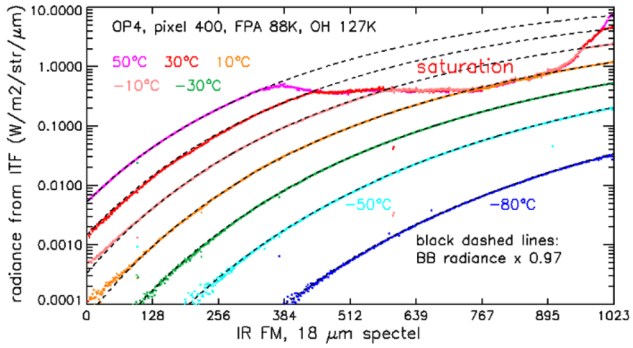

FIG. 23. Fit between radiances evaluated with the 1 MHz ITF and that expected from the Planck radiance for each blackbody temperature (black dashed line). For 1 MHz readout as for 100 kHz readout, significant residuals are only observed for connected spectels 0–100.

signal is ≤ 10 e^- so that with stacking (de-spiking, spatial, spectral, or frame averaging), it should be possible to evaluate signals lower than 5 e^-.

The two-dimensional 1 MHz ITF at the 18 μm level was determined using the same approach and the 100 ms reference integration time for 1 MHz readout. The saturation limit is reached for radiances eight times larger than with 100 kHz readout and its 800 ms integration time so that the fit with the Planck radiances is now observed over more than three orders of magnitudes (Fig. 23).

4. Corrections to be applied to the 2D ITF due to stray light contributions at short wavelengths

For the lower half of the wavelength range, the ITF was determined from spectral domains in the steep blue wing of the Planck curve. Even very minor spurious contributions from longer wavelengths can therefore impact radiometric calibration results. From 2850 to 5570 nm, the FPA is very effectively protected from such spurious contributions by the narrow spectral range of the LVF. From 2270 to 2850 nm, all photons within that wavelength range can reach the FPA through the bandpass filter, which protects it from high grating orders (at shorter wavelengths) and the thermal background (at longer wavelengths). With a 50 °C blackbody, there are 250 000 times more photons entering MAJIS with wavelengths 4500–5570 nm than legitimate photons with wavelengths 2283.2–2286.3 nm (single spectel near the short end of the wavelength range). Therefore, a contribution from long wavelength photons at 2285 nm can be significant even with a filtering efficiency of 10^{-6}. A spurious contribution can be identified as a signal that extends beyond the FOV after dark subtraction associated with a variation of the signal level within the FOV even with a flat source (blackbody inside the chamber or integrating sphere).

As shown in Fig. 24, the spatial profile of cold black bodies after dark signal subtraction in the LVF spectral range (blue line) is fully in line with expectations for a legitimate signal: no signal out of the FOV and a flat profile within the FOV (with minor vignetting, see Fig. 19). For hot blackbodies and short wavelengths (red and magenta curves in Fig. 24), there is a significant signal out of the FOV, with a trend to a larger total signal near the center of the FOV, which is a signature of a spurious contribution. This contribution, which reaches a level close to 50% of the total signal for the shortest wavelengths near the center of the FOV (see Fig. 24), needs to be modeled and subtracted so as to derive the ITF for the legitimate signal.

This task is made easier as the signals to the left and right of the FOV have a very similar spectral shape (see Fig. 25); hence, one can assume that the spurious contribution, which has a larger weight near the center of the FOV, keeps the same spectral profile as out of the FOV.

The weights for each pixel of the FOV have been evaluated with the procedure presented in Fig. 26 from the profile of spectel 5, for which the spurious contribution is largest. They can then be applied to the spectra of Fig. 25 to obtain spectra corrected from stray light for spectels 5–120 (the +50 °C range for radiometric calibration, see Fig. 18).

After correction from stray light, the spatial profiles for low wavelength spectels are now in line with the profile from the LVF range (see Fig. 27), a clear indication that the stray light correction procedure is effective. The 2D ITF can then be derived from the stray light corrected signal.

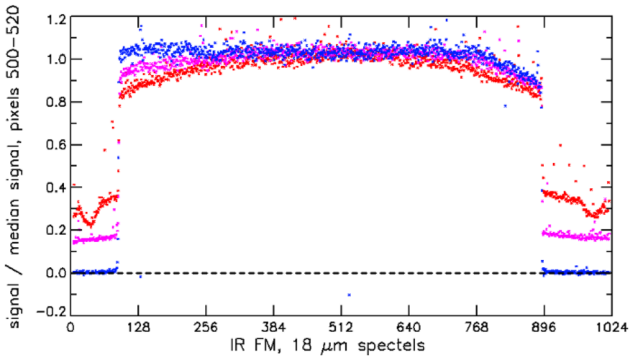

FIG. 24. Spatial profiles of spectel 400 (in the LVF range) with a blackbody at −50 °C (blue), and two spectels in the broadband filter range, spectel 10 (red) and spectel 50 (magenta) with a blackbody at +50 °C. The two dips out of the FOV for spectel 10 correspond to positioning marks on the filter.

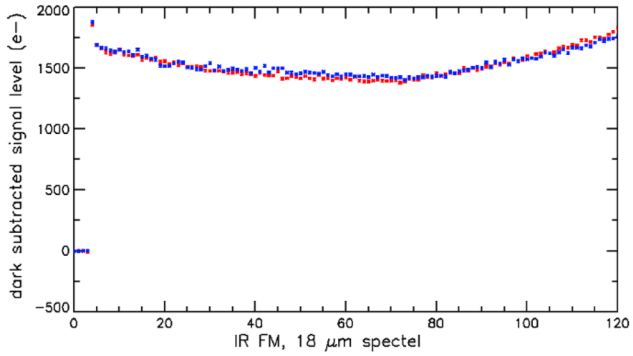

FIG. 25. Signals with a 50 °C blackbody 10 pixels left (blue) and 10 pixels right (red) of the edges of the FOV in the spectral range over which the 50 °C blackbody has been used for radiometric calibration.

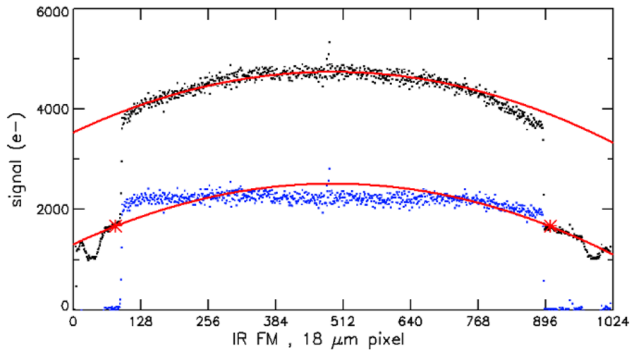

FIG. 26. Black dots: Spatial profile of spectel 5 (lowest wavelength not impacted by spillover; see Sec. II E). A parabolic fit (red curves) works well for both the signal in the FOV and the signal out of the FOV, with a near constant offset corresponding to the legitimate signal, expected to be flat. The legitimate signal (blue dots) has been evaluated by subtracting the spurious signal determined at the two reference locations close to the edge of the FOV (red stars) with a coefficient defined by the parabolic fit.

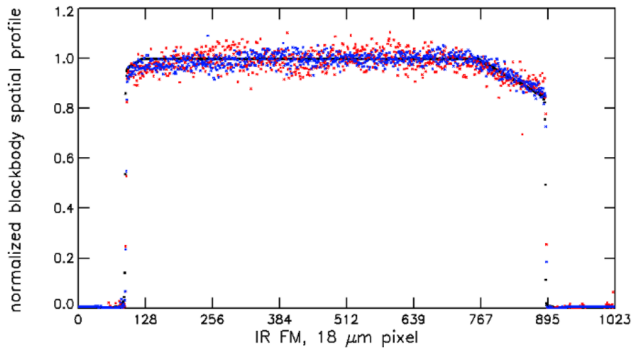

FIG. 27. Spatial profiles of spectels 10 (red) and 50 (blue) normalized to the median signal for pixels 400–600 compared with the vignetted flat signal from Fig. 19 (black) derived from profiles in the LVF spectral range.

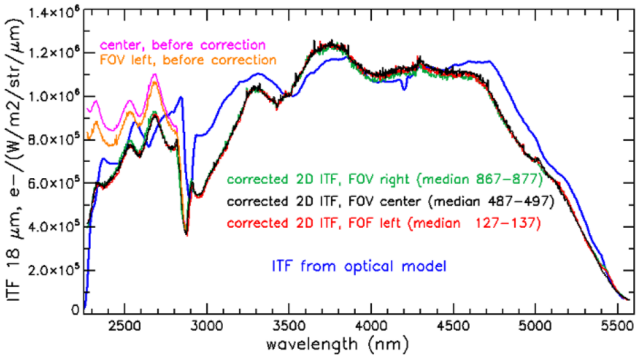

FIG. 28. Median instrument transfer function for the IR channel for 18 × 18 μm^2 H1RG pixels determined before and after removing spurious contributions in the bandpass filter range (2270–2850 nm) at three locations in the FOV.

After correcting for the stray light contribution, the ITFs at the left edge, center, and right edge of the FOV are very similar (Fig. 28). They are also in very good agreement with a model ITF (blue curve in Fig. 28) combining the optical performance of the OH with the transmission of the two filters and the wavelength dependence of the quantum efficiency. The discrepancy for the dip at ~2850 nm results from a slightly higher setting of the broadband filter edge at the time of the modeling.

For calibration sources with a higher color temperature such as a QTH lamp both as an external source and as one of the two sources of the Internal Calibration Unit (ICU), there are more photons at short wavelengths than at long wavelengths; hence, the stray light contribution in the broadband filter spectral range is negligible, with very low signal levels out of the FOV. This made it possible to reduce the pixel to pixel dispersion of the ITF at short wavelengths by evaluating high frequency variations with sources free of stray light.

Scattered sunlight has a color temperature ~5900 K so that short wavelength stray light is not an issue for most observations with the IR channel. Some caution may, however, be required for interpreting the short wavelength range of spectra of "hot spots" on the night side of Jupiter for which photon fluxes at long wavelengths are much larger than that at short wavelengths.

5. Evolution of the 2D ITF with the temperature of the FPA

A key question for science operations was whether the 2D ITF measured with a FPA IR at a temperature of 88 K could be used for other operating temperatures of the FPA IR. The characterization of the IR FM detector showed that for most pixels, the conversion efficiency exhibited only very minor dependence with temperature (see Sec. II D). Conversely, higher temperatures and/or longer integration times result in an increase in the proportion of non-operable ("hot") pixels (see Sec. II E).

Figure 29 shows the comparison of the signals obtained with the FPA in 100 ms at 100 and 88 K (Fig. 29, top panel) with the same source (blackbody at +10 °C) after applying linear correction and dark signal subtraction. They cover a dynamic range of 1000 for wavelengths up to 4000 nm (at longer wavelengths, the signal

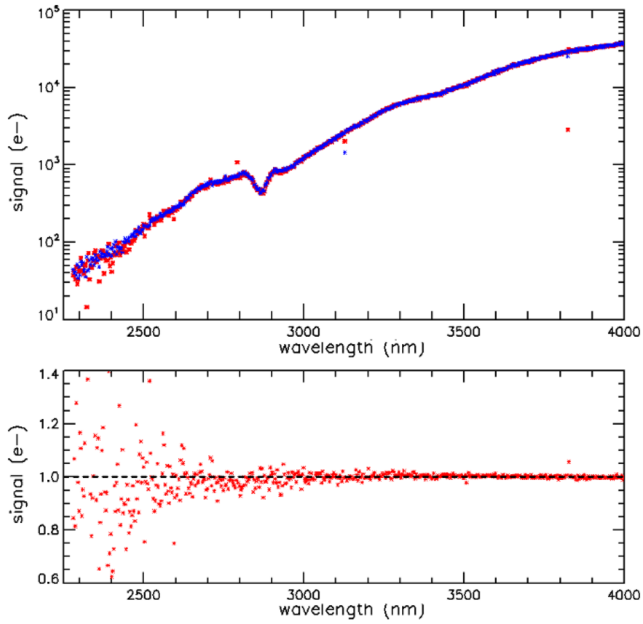

FIG. 29. Top panel: Dark-subtracted signal (16 frames average) for 18 μm pixel 512 of the IR FM detector with the blackbody at +10 °C for an integration time of 100 ms (1 MHz readout) up to 4000 nm. The blue and red dots correspond to a temperature of the FPA of 88 K (blue) and 100 K (red).The stragglers correspond to unreliable hot spectels. Bottom panel: Ratio between the signal measured with the detector at 100 K and 88 K.

reaches saturation). The ratio of the signals at 100 and 88 K (Fig. 29, bottom panel) is close to 1 with a dispersion in line with the noise model. At the shortest wavelengths, the SNR is poor even with an average of 16 frames as the signal is low (< 100 e^-) with a large readout noise (30 e^- at 1 MHz) and a significant shot noise contribution from the dark current at 100 K, which reaches ~500 e^- in 100 ms. This shows that the ITF-2D as derived with the detector at 88 K can be used at wavelengths < 4000 nm when the detector is at 100 K. It is important to note that with an integration time of 100 ms, the IR channel still provides reliable data at a temperature of 100 K, well beyond the operating range (88–96 K) expected during science observations from MAJIS thermal modeling.

The determination of radiances using the 88 K 2D ITF for hot detector temperatures was checked at longer wavelengths by comparing the radiance for a blackbody with the Planck function weighted by the setup optical transmission. As shown in Fig. 30, the fit with Planck radiances when applying the 88 K ITF to signals measured with the FPA at 100 K is excellent up to ~5100 nm, with a small slope indicating that the blackbody temperature may have been a fraction of a °C higher for the observation with the FPA at 100 K when compared to the observation with the FPA at 88 K. The lower radiance at 100 K beyond 5100 nm is due to a decrease in the cutoff wavelength with temperature, which results in a lower quantum efficiency close to the cutoff wavelength.[22] For an FPA temperature of 100 K, the loss in conversion efficiency from 5100 to 5500 nm can be modeled with a cutoff wavelength of 5.63 μm at 88 K near the long wavelength edge of the FPA decreasing to 5.56 μm at 100 K.

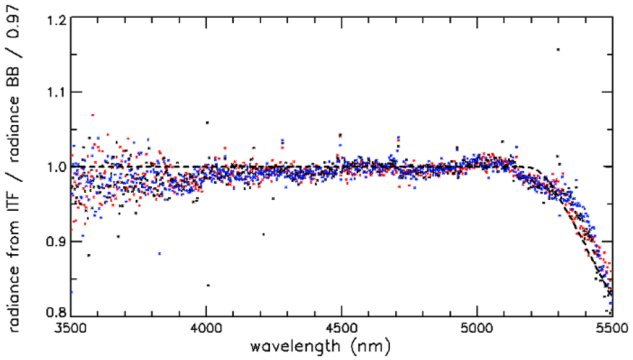

FIG. 30. Comparison of the Planck radiances (×0.97) with the radiances determined for 18 μm pixels 150 (blue dots), 510 (black dots), and 850 (red dots) for a blackbody at −80 °C with 1 MHz readout, an integration time of 100 ms, and the FPA at 100 K. The radiances have been evaluated using the 2D ITF for 1 MHz readout determined at 88 K. The black dashed curve corresponds to the results of a model[18] for the decrease in the quantum efficiency close to the cutoff wavelength of a detector.

Therefore, a single 2D ITF can be used under all operating conditions if associated with an operability mask dependent on temperature and integration time, which indicates which H1RG pixels are still reliable under these operating conditions (see Sec. II E). As

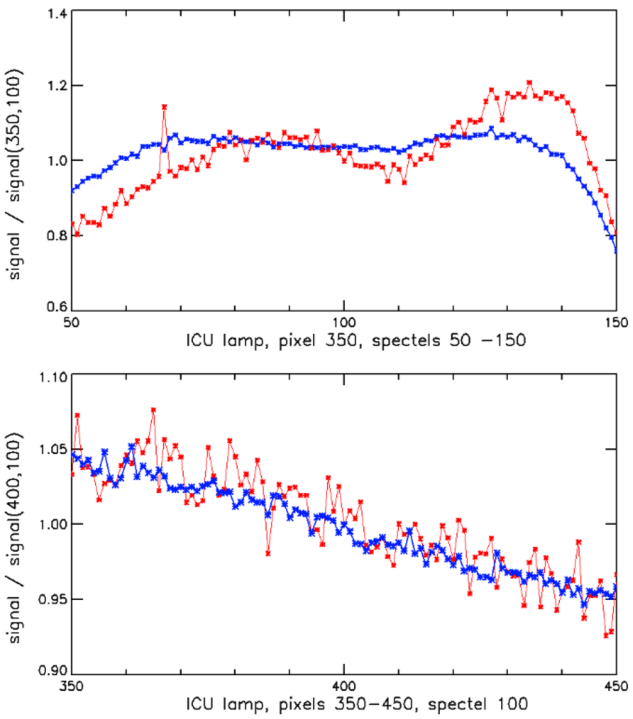

FIG. 31. Spectral profile (top panel) and spatial profile (bottom panel) of a normalized signal with the QTH lamp of the Internal Calibration Unit (ICU) of MAJIS. The red dots correspond to the signal in DNs, and the blue dots correspond to the signal once converted into radiances using the 2D ITF. The detector temperature was 88 K, and the integration time was 80 ms (1 MHz readout).

shown in Fig. 30, the adjustment that needs to be implemented for a FPA temperature of 100 K (beyond the expected operational range) at wavelengths >5.1 μm can be modeled as a function of the temperature of the FPA. It can be noted that the largest signals at such wavelengths are that from Jupiter observations (cold case, for which the 2D ITF can be applied as such), while the SNR from icy satellites with an integration time of 100 ms (hot case) is expected to be very low so that there is only a minor impact if the adjusted 2D ITF is slightly off.

As discussed in Sec. II D, high frequency variations in the 1.5% range are observed between detector pixels. Applying a 2D ITF derived to a blackbody (which should be inherently very flat) to signals from other sources was expected to reduce this jitter in both the spectral and spatial directions once the linearly corrected DNs have been converted into radiance units. As shown in Fig. 31, this is indeed the case for the spectral profile, even for warm spectels such as spectel 67, which is close to saturation with a signal ~50 000 e^-. The residual dispersion of radiances is also reduced to ~0.5%, for the spatial profile, most impacted by pixel to pixel variability as it combines that from the IR FPA with small variations in the width of the slit, which will be further discussed in Sec. III D.

D. Radiometric calibration of the VISNIR channel

1. The VISNIR stray light issues

Stray light issues were identified in the VISNIR channel, with an impact on radiometric calibration. The most straightforward identification was made when observing the blackbody inside the calibration chamber used for radiometric calibration of the IR channel (see Sec. III B) with the VISNIR channel. The blackbody was at a temperature of 80 °C, the maximum temperature acceptable in the vacuum chamber.[2] At this temperature, the signal was expected to peak near the upper end of the VISNIR wavelength range (491–2360 nm[4]). As shown in Fig. 32, the signal at wavelengths longer than 1300 nm follows the expected pattern, with a rapid increase in the Planck curve with wavelength until 2200 nm, beyond which the signal decreases due to the rapid decrease in the reflectivity of the dichroic with wavelength in this spectral range (see Sec. III A). The minor vignetting of the blackbody signal identified with the IR channel is also observed with the VISNIR channel at pixels 875 (right side of the FOV) and 110 (left side of the FOV) when compared to the center of the FOV (pixel 512).

However, signals totaling more e^- than the expected signal were also observed at shorter wavelengths. As the radiance of a blackbody at 80 °C is very close to 0 at these wavelengths, these signals can only result from long wavelength photons reaching the regions of the FPA corresponding to short wavelengths as stray light. As discussed in Sec. III A, all photons with wavelengths smaller than 2250 nm and a small fraction of longer wavelength photons are reflected to the VISNIR spectrometer by the beam splitter. The VISNIR FPA is covered by a high bandpass LVF for excluding high grating orders, which means that all photons with wavelengths lower than the VISNIR cutoff (~2550 nm) and larger than ~70% of the wavelength corresponding to a spectel can be converted to electrons.

This stray light signal is largest in the center of the FPA (pixel 512). As shown in Fig. 32, it decreases faster toward the low end of the FOV (pixel 95) than toward the high end of the FOV (pixel 894). The spectral profile of the stray light changes with location.

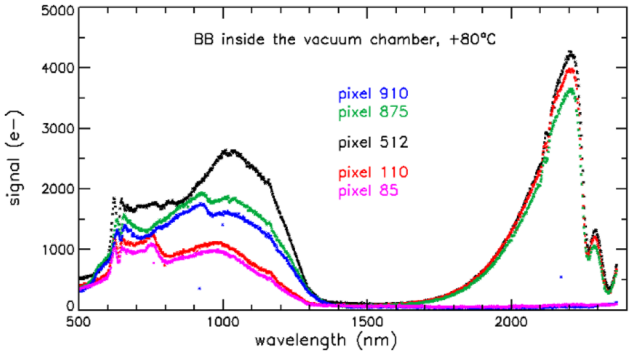

FIG. 32. Blackbody at 80 °C observed by the VISNIR with an integration time of 2 s at the center (pixel 512), close to the edges (pixels 110 and 875), and beyond the edges (pixels 85 and 910) of the VISNIR FOV with the blackbody inside the vacuum chamber at a temperature of 80 °C. Large spurious contributions are observed at wavelengths shorter than 1300 nm in the FOV and beyond the edges of the FOV, peaking near the center of the FOV (pixel 512).

The stray light signal extends beyond the edge of the FOV (pixel 85 and 910) with spectral shapes similar to that for nearby pixels in the FOV (pixels 110 and 875) and a slightly lower intensity. These characteristics indicate that each location in the entry slit generates a spatially extended contribution to the stray light, which explains why it is largest in the center, while slowly decreasing beyond the edges of the FOV.

The signal out of the FOV shows that there is a small stray light contribution at wavelengths larger than 1300 nm. It becomes quite significant beyond 2250 nm as the legitimate signal rapidly decreases with the reflectivity of the beam splitter (see Fig. 32).

A detailed analysis of calibration results provided important clues on the origin of this stray light. As expected, the stray light relative weight increases with the spatial extent of the source as more slit positions contribute to the stray light so that extended sources such as the internal blackbody constitute a worst case. Extended sources with higher color temperatures such as the IR ICU (when observed with the VISNIR channel) and the ICU lamp provide a legitimate signal in the 500–1350 nm spectral range for pixels within the FOV, but the stray light can still be investigated from the signal for pixels outside the FOV. It should be noted that part of the stray light at very short wavelengths does not go through the slit as it is observed when the shutter is closed. The spectral profile of the stray light contribution is very similar whatever the color temperature of the source both beyond the left edge of the FOV and beyond the right edge of the FOV (Fig. 33).

Stray light at short wavelengths was also observed with monochromatic sources but only for wavelengths from 1000 nm up to the upper end of the VISNIR spectral range, wavelengths near the upper end of the visible spectral range providing the largest contributions. This was confirmed by observations with the blackbody inside the vacuum chamber at lower temperatures than 80 °C: the level of the stray light scales as the radiance at ~2000 nm, which means that the spectral distribution of stray light photons is centered at this wavelength.

Observations of sources with a small angular size when positioning the line of sight at different angles in the cross-slit direction

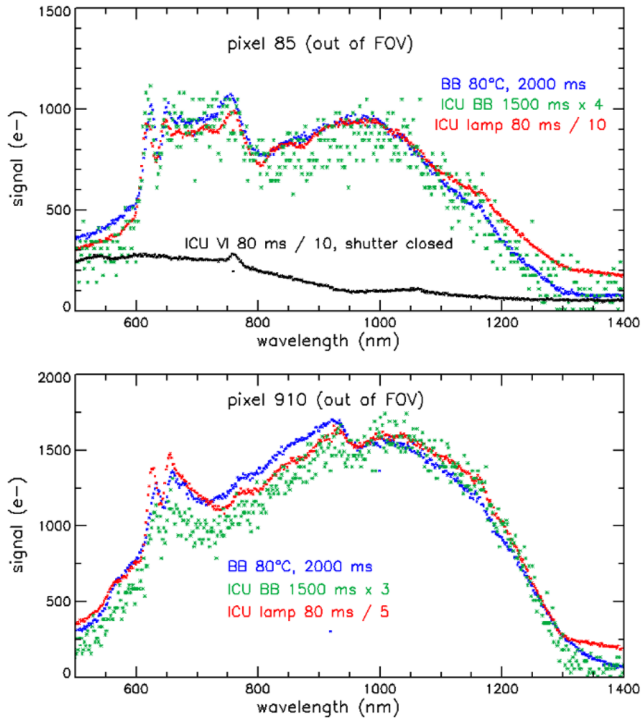

FIG. 33. Spectral shape of the stray light near the left edge of the FOV (top panel, pixel 85) and near the bottom edge of the FOV (bottom panel, pixel 910) for three extended sources with color temperatures ranging from ~80 °C (BB) to ~2780 °C (ICU QTH lamp).

with respect to the source showed that the wide spectral profile of the stray light with an extended source was generated by contributions shifting in wavelength with the cross-slit angle. An example is provided in Fig. 34 with a hot blackbody external to the thermal vacuum chamber (spatial dimension: ~60 pixels in the along-slit direction and ~40 pixels in the cross-slit direction).

The blackbody radiance is much larger at 250 °C than that at 80 °C (by a factor close to 500 at 2140 nm). However, the stray light

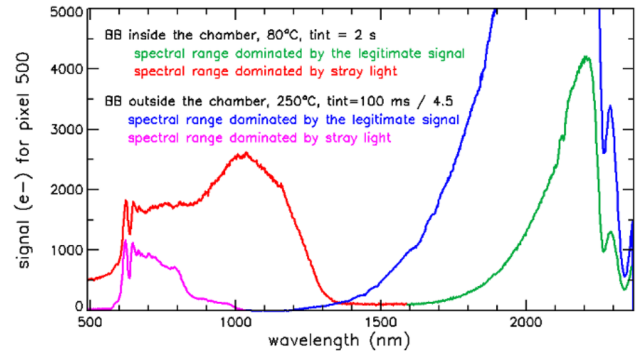

FIG. 34. Signal at the center of the FOV for the internal blackbody (covering the full FOV) at 80 °C and from a hot blackbody outside the chamber (covering 40 × 60 pixels) at 250 °C positioned at the central position in the FOV.

at short wavelengths is much smaller compared to the legitimate signal with the hot external blackbody than for the blackbody covering the full FOV due to the limited spatial extent in the along-slit direction. Furthermore, due to the limited spatial extent in the cross-slit direction, the stray light contribution covers a smaller spectral range (600–1000 nm) than with an extended source (the scaling factor of 4.5 for the external blackbody in Fig. 34 has been selected to provide a similar "double peak" structure between 600 and 650 nm).

2. Determination of the VISNIR ITF for wavelengths >1000 nm with an external blackbody

The smaller impact of stray light on the dataset using the external blackbody made it possible to perform a radiometric calibration of the legitimate contribution near the center of the FOV for wavelengths larger than 1000 nm by using the external blackbody as a reference. A scaling factor depending on wavelength needs to be applied to the blackbody radiance due to the six reflections on aluminum mirrors in the optical bench and the transmission of the vacuum window chamber. Temperatures higher than 250 °C are needed for improving the SNR at wavelengths ranging from 1000 to 1400 nm.

As expected, the spatial profiles of the signal from the external blackbody (Fig. 35) are much wider in the stray light dominated spectral range than in the spectral range dominated by the legitimate signal, with a very smooth spatial profile for the stray light. Therefore, similarly to what was done for the short wavelengths of the IR channel (see Sec. III B), stray light in the central area can be modeled from the stray light signal observed out of the central area (e.g., pixels 440 and 460, red dashed lines in Fig. 35).

As shown in Fig. 36, this approach is effective up to a temperature of 425 °C of the external blackbody. This made it possible to evaluate radiometric performance down to 1000 nm for the legitimate contribution. The stray light contribution increases by a factor of ~10 when the wavelength becomes smaller than 1000 nm so that the subtraction becomes unreliable at shorter wavelengths. Therefore, the external blackbody has been used for defining the ITF of the VISNIR channel of MAJIS relevant for the legitimate signal

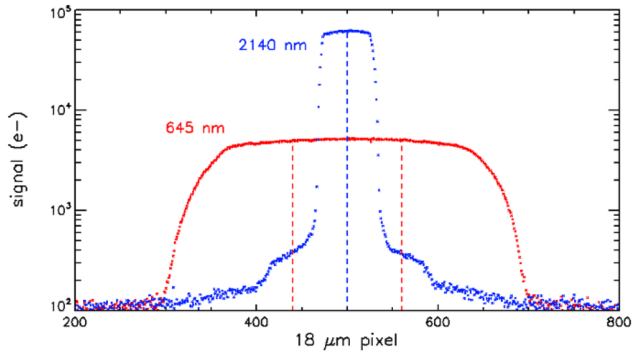

FIG. 35. Spatial profiles in log scale of the external blackbody at 250 °C for a spectel corresponding to a wavelength of 2140 nm (blue) dominated by the legitimate signal and for a spectel corresponding to a wavelength of 645 nm (red) dominated by stray light. The two dashed lines indicate the locations that have been used as references for modeling the stray light.

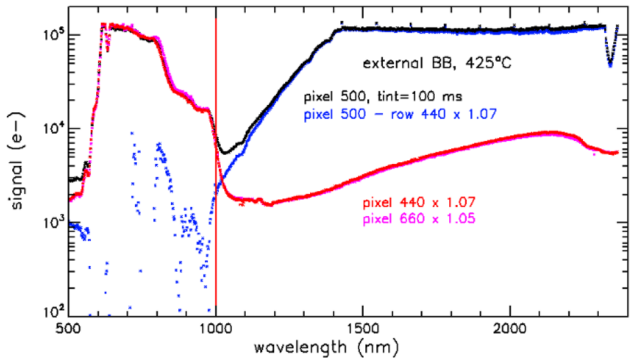

FIG. 36. Signal for pixel 500 with the external blackbody at 425 °C (black) and an integration time of 100 ms. The stray light contribution can be modeled from that observed for pixels 440 and 660 (red and magenta) and subtracted, which makes it possible to evaluate a legitimate signal (blue) increasing from ~2000 e^- at 1000 nm to saturation (~105 000 e^-) at 1400 nm.

from 1000 nm to the upper end of the VISNIR wavelength range (2365 nm) in the center of the field of view.

3. Modeled ITF for wavelengths lower than 1000 nm

As shown in Figs. 36, 37, and 39, the spectral profile of the stray light contribution is similar for pixels in the same area of the FPA. Near the edges of the field of view, this makes it possible to model the stray light contribution from the signal observed on pixels out of the field of view, with no legitimate signal. This provided a path for assessing the instrument transfer function in the spectral range from 490 to 1000 nm from spectra obtained with the ICU lamp, which presents four deep didymium absorption lines in this spectral range. With this source, the expected signal level at the shortest wavelengths is very low so that most of the observed signal is contributed by stray light, which makes it possible to estimate a scaling factor for stray light between positions within and out of the FOV as presented in Fig. 37.

As shown in the bottom panel of Fig. 37, subtracting a scaled stray light contribution from the signal of pixels close to the edge of the FOV provides a very good match between legitimate signals near both edges of the FOV with a constant factor of 2.12, which is in line with the ICU lamp signal ratio measured with the IR channel (ratio of 2.1). This scaling factor applies to spectels 430–950, where the stray light is small, as well as for spectels 0–430, where it represents a major contribution, larger near the right edge than the left edge of the FOV.

The ICU lamp has been measured at Leonardo Company (LDO) by a spectrophotometer,[6] which provides a reference for the spectral profile of the radiance of this light source (the absolute level depends on the view factor of the scattering screen, which varies across the FOV). A model ITF was evaluated before the calibration campaign on the basis of the optical efficiency of the optics, the transmission of the VISNIR high pass LVF, and the quantum efficiency as derived from FPA characterization. Applying this model ITF to the legitimate signals of Fig. 37 in the 500–1000 nm spectral range provided radiances that could be compared to the spectral profile of the ICU lamp measured by LDO (Fig. 38). The relative spectral evolution of the radiance of the legitimate signal closely matches

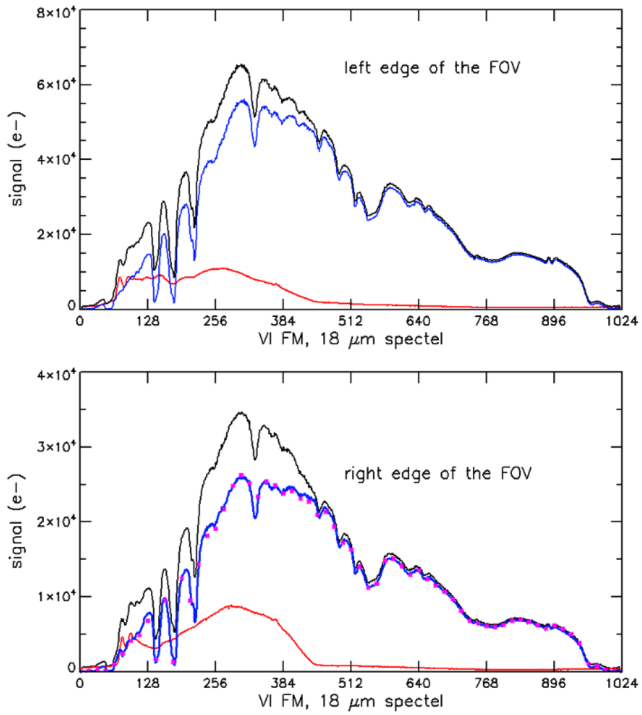

FIG. 37. Top panel, black line: Signal measured with the ICU lamp for pixel 120 (black, close to the left boundary of the VISNIR FOV, at pixel 97); red line: modeled stray light for pixel 120 = signal of pixel 85 (beyond the left edge of the FOV) scaled by a factor 1.15; and blue line: legitimate signal = total signal − model stray light. Bottom panel, black line: Pixel 875 (close to the right of the FOV, at pixel 896); red line: modeled stray light for pixel 875 = signal of pixel 910 (beyond the right edge of the FOV) scaled by a factor 1.12; and blue line: legitimate signal = total signal − modeled stray light. The magenta dots overlying the blue line in the bottom panel correspond to the ICU legitimate signal of pixel 120 (blue line in the top panel) divided by a factor 2.13 and sampled every 16 spectels.

that obtained with the spectrophotometer measurements for both the continuum and four deep didymium absorption bands, with (as expected) better defined spectral profiles with MAJIS than with the LDO spectrophotometer.

On this basis, the model ITF has been considered as adequate for defining the ITF relevant for the legitimate signal below 960 nm. This is confirmed by the relatively close agreement of this model ITF and the ITF derived from calibration measurements at 1000 nm (factor of 1.075). As already mentioned, the ITF relevant for the legitimate signal has been derived from calibration measurements for wavelengths longer than 1000 nm.

As shown in Fig. 39, the spectral profiles of the measured and model ITF for the legitimate signal are similar within 20% from 1000 to 1800 nm. The measured throughput is higher than the model ITF by a factor of 1.2–2.3 from 1800 to 2200 nm, which is beneficial for MAJIS science objectives as there are diagnostic signatures of salts and acid brines expected on icy satellites in this spectral range.

All these measurements have been performed with the 1 MHz readout. The same ITF has been considered as applying to 100 kHz readout, applying the appropriate conversion efficiency to 1 MHz and 100 kHz data (factor of 16/15.54, see Sec. II C) for deriving the

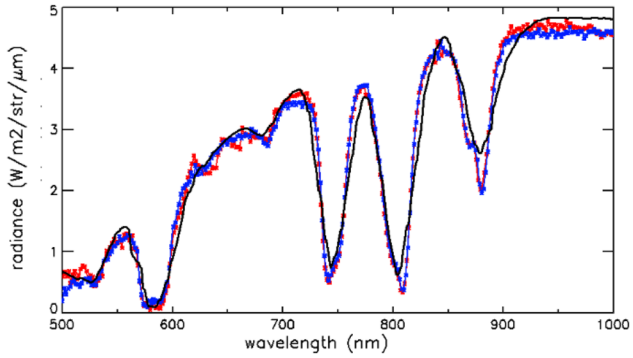

FIG. 38. Radiance of the legitimate signal evaluated from the MAJIS spectrum at row 120 (red) and row 878 (blue, with a scaling factor of 2.03) after subtracting a modeled stray light contribution and applying the model transfer function. The black line corresponds to the radiance measured at LDO scaled to provide the best fit with MAJIS results.

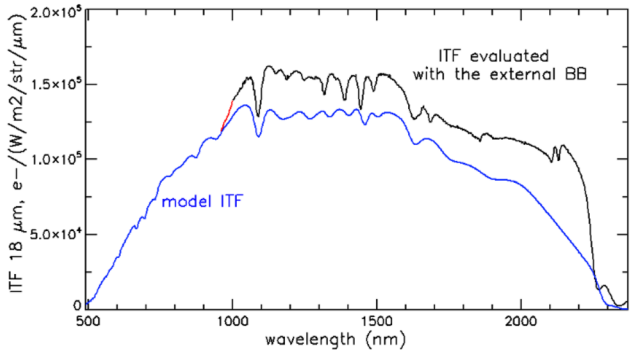

FIG. 39. VISNIR ITF as measured during calibration for wavelengths larger than 1000 nm (black) and extended to wavelengths lower than 960 nm using the model ITF (blue). A coefficient increasing from 1 to 1.075 has been applied to the model ITF between 960 and 1000 nm so as to bridge the small gap between the two evaluations (red line).

throughput in terms of linearity corrected DNs. The main difference between the two readout modes is the larger well depth with 1 MHz readout, which applies to both the VISNIR[18] and IR[16] channels. The mismatches between the two readout modes observed for the IR channel when the signal gets close to saturation never exceed a few percentage, which is smaller than the uncertainties on absolute radiometry of the legitimate signal introduced by stray light subtraction.

4. Testing the validity of the VISNIR ITF

A first test of the validity of the VISNIR ITF in the upper part of the VISNIR wavelength range can be made by applying the stray light subtraction approach to data obtained with the blackbody inside the vacuum chamber close to an edge of the FOV (Fig. 40). The peak signal ~ 4000 e^- was obtained with an acquisition time of 2 s. A good fit is obtained between the legitimate signal and that expected by applying the ITF to the radiance of the blackbody inside the vacuum chamber (with a factor of 0.97, see Sec. II).

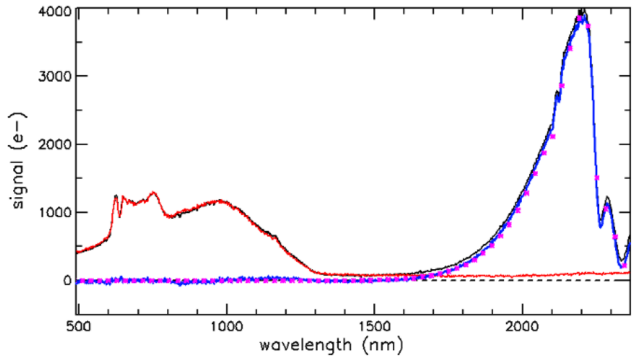

FIG. 40. Signal for pixel 120 with the blackbody source inside the chamber at a temperature of 80 °C before (black) and after (blue) subtracting a modeled stray light contribution (red) derived from the signal on pixel 85, out of the FOV, by applying a factor 1.2 to fit the stray light contribution below 1000 nm. The magenta dots correspond to the signal expected when applying the VISNIR ITF to the blackbody radiance (×0.97).

A second check on the validity of the VISNIR ITF is the consistency in terms of spectral profile between the VISNIR spectral range and the IR spectral range using the ICU extended source. As shown in Fig. 41, the radiances are consistent at the boundary between the

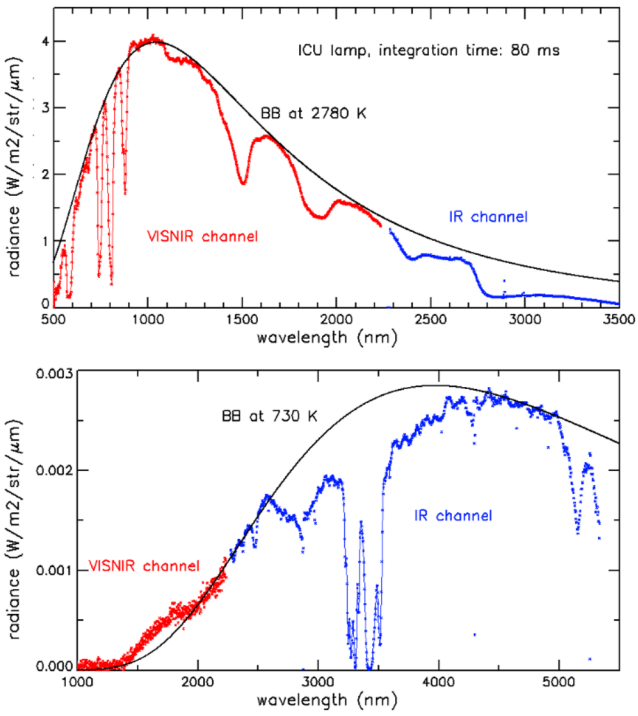

FIG. 41. Radiance profile obtained with both channels for the ICU lamp (top panel) and the ICU blackbody (bottom panel) after subtracting a modeled stray light contribution in the short wavelength range of the VISNIR channel. The observed radiance profiles indicate color temperatures in the range of 2780 K for the ICU lamp and 730 K for the ICU blackbody. The signal from the ICU blackbody is very low in the VISNIR channel.

two channels for both the ICU lamp and the ICU blackbody (with low signal levels and hence low SNR in the VISNIR channel for the latter).

5. 2D VISNIR ITF

At this stage, a single ITF has been defined, applying to the central region of the FOV derived from external blackbody data for wavelengths larger than 1000 nm (Sec. III B 2) and from a model ITF for wavelengths smaller than 1000 nm (Sec. III B 3). The inter-pixel variability for the FM VISNIR FPA is very small (0.7%, see Sec. II B) so that the main contribution to a 2D ITF comes from large scale variations, which have been determined with flat sources (internal blackbody and QTH lamp + integrating sphere).

As shown in Fig. 42, the spatial profile for a blackbody at 80 °C as observed by the VISNIR channel is very similar to the IR profile for the same blackbody at lower temperatures, with a deficit in signal by a few percentage at the left of the FOV.

One can note that there also seems to be a match between small variations at high spatial frequencies. This is confirmed by magnifying the region from pixel 600 to pixel 700 (Fig. 43). There is a clear correlation between the high frequency variations of VISNIR spectels. Furthermore, the median profiles of 31 spectels for the VISNIR and IR channels closely match after applying the 8 pixels offset, which is required for a match between the edges of the two FOVs at these wavelengths. As it applies to both channels, this correlated variability at high spatial frequencies can be attributed to small variations of the effective slit width (nominally 36 μm) along the slit. This high resolution (HR) pattern has been applied to the VISNIR ITF at all wavelengths after applying the observed shift in position of the edges of the FOV between each wavelength and the reference wavelength (spectels 910–940 and 2140–2196 nm).

A mapping at median spatial scales of the 2D ITF relative to that in the center of the FOV as determined from Sec. III B 2 ($\lambda > 1000$ nm) and Sec. III B 3 ($\lambda < 1000$ nm) has been generated from median values over 20 pixels of an average of 16 frames obtained with the OH at 126 K (cold case) with the external blackbody at 80 °C. This provides an SNR > 100 for wavelengths larger than 2000 nm. For wavelengths ranging from 1300 to 2000 nm, where the stray light contribution is small, the same approach has been used with data from an integrating sphere illuminated by a QTH lamp for evaluating small variations in the spectral response. At wavelengths shorter than 1300 nm, the ITF has only been adjusted for medium scale and HR spatial variations as variations of the spectral response (never exceeding 2% from 1300 to 2000 nm) become unreliable.

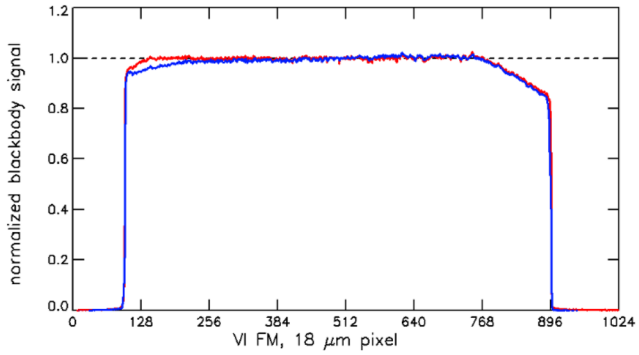

FIG. 42. Median normalized profile of the TVC blackbody at 80 °C for VISNIR spectels 910–940 (blue) compared to that of the blackbody at −80 °C as observed by the IR channel (red, median of IR spectels 350–380). The IR profile has been shifted left by 8 pixels so as to match the edges of the FOV as observed by both channels.

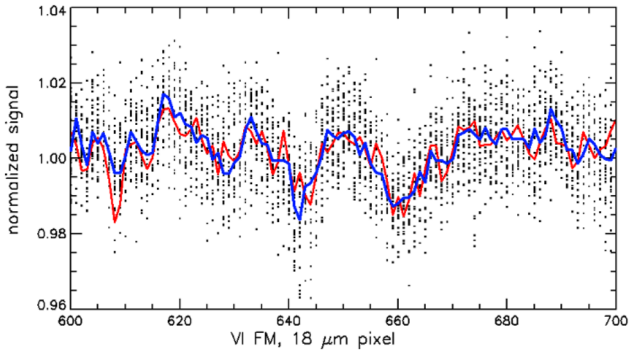

FIG. 43. Magnified view of the spatial profiles of Fig. 42 for pixels 600–700. The black dots correspond to the normalized VISNIR signals for the 31 spectels from 910 to 940. The blue and red profiles correspond to the median normalized profiles for the VISNIR channel and IR channels as in Fig. 42.

The VISNIR detector is at a temperature close to that of the optical bench of the OH. A comparison between calibration data obtained in the cold case and the hot case (OH temperature: 137 K) did not reveal significant differences in the radiometric response so that similarly to the IR channel, the 2D VISNIR ITF can be used at all FPA-temperatures in the expected operating range.

As for the IR detector, an operability mask has to be applied to screen out dead, hot, and unreliable H1RG pixels. As discussed in Sec. II E, the operability of the VISNIR FPA is above 99.5% at the level of H1RG pixels (18 μm) for the 125–132 K range of expected operating temperatures of the VISNIR FPA so that the operability mask will have only a minor impact on science observations.

6. Impact of the VISNIR stray light on MAJIS science observations

Subtraction of a modeled stray light contribution is reliable for pixels close to the edge of the FOV (or to the edge of the illuminated part of the slit if the FOV is not fully covered). However, such an approach is not available for most of the FOV, and it will not be available in flight when the target covers the full FOV, as windowing will restrict the collected data to the FOV for the nominal acquisition mode. It is therefore important to assess the impact of stray light contributions at wavelengths shorter than 1300 nm on MAJIS science observations.

The observations performed with the ICU lamp make it possible to obtain information on the relative weight of the stray light with respect to the total signal at several wavelengths in the 500–1300 nm range for a source with a color temperature of ~2780 K. The spectral profiles obtained after stray light subtraction near both edges of the FOV (Fig. 38) are very consistent with measurements of the transmission of the ICU didymium coating in the lab. The band depth of didymium absorption bands centered at 581, 738, and 807 nm are very deep. Stray light contributions result in a loss of spectral

contrast for absorption bands so that the proportion of legitimate photons at these three wavelengths can be derived across the full FOV by comparing the measured band depth for each of the absorption bands at each pixel location with the band depth of the lab measurements (Fig. 44). It ranges from 60% to 80% depending on wavelength and location. The results of a similar analysis performed on samples with strong spectral features[5] are consistent with that obtained with the ICU.

For MAJIS science observations, the observed signal in the VISNIR wavelength range will result from scattering of solar photons. As stray light at short wavelengths is generated by photons with wavelengths in the upper part of the VISNIR range, the contribution of legitimate photons to the total signal at short wavelengths is expected to be larger with sunlight (color temperature ~5800 K) compared to that with the ICU lamp (color temperature ~2780 K).

As shown in Fig. 45, the contribution of photons from the legitimate signal should improve by a factor of more than 3 with respect to stray light at wavelengths shorter than 1000 nm and by a factor of more than 10 at wavelengths shorter than 700 nm compared to the observations with the ICU lamp. On this basis, one can derive the expected contribution of the legitimate signal to the total signal with sunlight from that observed with the ICU.

As shown in Fig. 46, for MAJIS observations of Jupiter or icy satellites, the loss of spectral contrast due to stray light should not exceed 10% for wavelengths ranging from 581 to 807 nm. The loss of contrast should not exceed a few percentage at 581 nm due to the very large increase in the photon flux at this wavelength between 2780 and 5800 K (by a factor of 25, see Fig. 45) when compared to the source region of the stray light centered at 2000 nm. It should, however, be noted that most of the stray light at very short wavelengths does not go through the slit; hence, it is much reduced by subtracting the "shutter closed" signal, but this requires that this signal is representative of the out of slit stray light during the observation. The broad absorption band of H_2O ice centered at 2000 nm should further reduce the loss of spectral contrast due to stray light for Europa and to a lesser extent for Ganymede. Furthermore, as shown in Figs. 33 and 34, stray light contributions exhibit very specific spectral signatures for a wide range of color temperatures of the source. Therefore, the stray light contribution may be further evaluated and mitigated on the basis of the strength of spectral features specific to stray light, such as the double peak at 630 and 690 nm.

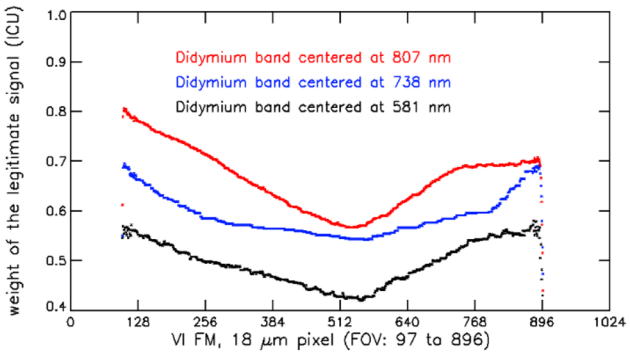

FIG. 44. Contribution of legitimate photons to the total signal evaluated after launch from the measured band strength at three wavelengths corresponding to deep didymium absorption bands of the ICU lamp centered at 581, 738, and 807 nm.

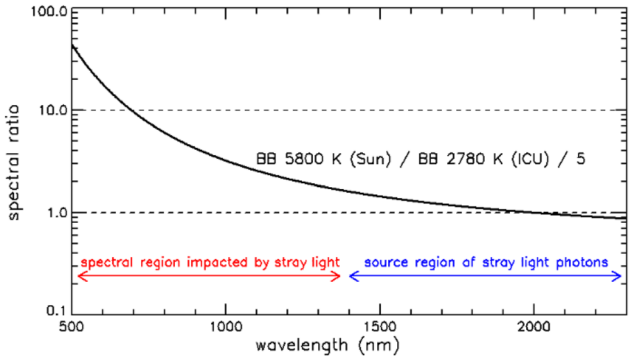

FIG. 45. Relative increase in the legitimate signal with respect to stray light with solar photons compared to the ICU lamp as a function of wavelength. The photon flux ratio between 5800 and 2780 K is ~5 in the source regions of stray light photons, centered at 2000 nm. It reaches 50 for a wavelength of 700 nm.

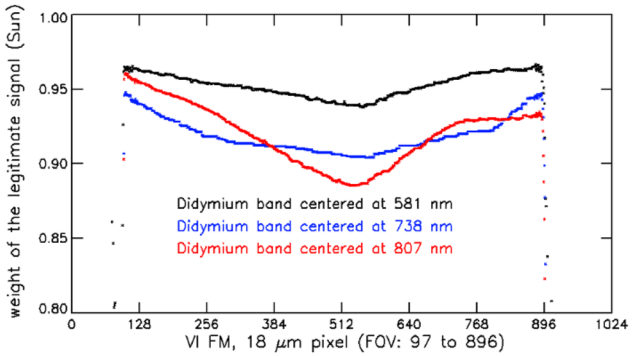

FIG. 46. Estimated contribution of legitimate photons to the total signal with sunlight at three wavelengths corresponding to deep didymium absorption bands centered at 581, 738, and 807 nm.

Given the sharp drop of signal beyond 2250 nm, observations of representative samples[5] led to the conclusion that a reliable evaluation of spectral features could only be considered up to 2200 nm until the stray light contribution at these wavelengths can be modeled.

On the basis of this analysis, the impact of stray light on the interpretation of MAJIS observations at VISNIR wavelengths shorter than 1300 nm, while significant, should be manageable. It is important to validate this conclusion with actual measurements obtained on targets illuminated by sunlight. They are also required for assessing the impact of stray light at long wavelengths larger than 2250 nm, as it is 4% larger with the ICU lamp than with an 80 °C blackbody so that it may further increase with sunlight. The most favorable opportunities consist in observing the sunlit part of the Moon from distances of 600 000 to 800 000 km during the Earth flybys (first opportunity: August 2024) using a cross-slit scan for investigating the full spectral profile of stray light. At such distances, the lunar disk will cover 30–40 nominal MAJIS pixels (150 μrad).

The observations will be performed without spatial binning (lunar disk: 60–80 detector pixels) so that they can be directly compared to calibration results. This will make it possible to resolve maria (visible albedo ~10%) and continents (visible albedo ~20%). With windowing (128 detector pixels) and an integration time of 10 ms, the signal should not exceed the well depth even for continents, and observations scanning across the lunar disk at different positions in the FOV will make it possible to monitor the stray light contribution in a configuration similar to that of the external blackbody (60 pixels wide along-slit and 40 pixels cross-slit). Observations during the close approach of the Moon will also be of interest for evaluating the VISNIR stray light with a sunlit source covering the full FOV.

Spectral characteristics in the visible and near IR of specific lunar regions are well known from observations with lunar orbiters so that MAJIS observations of the Moon during the two Earth flybys will also make it possible to consolidate the MAJIS VISNIR ITF for legitimate signals from calibration at wavelengths longer than 1000 nm while obtaining a first check of the MAJIS VISNIR ITF at wavelengths shorter than 1000 nm, which was derived from modeling. These observations will therefore be critical for confirming that the legitimate signal contribution is much improved for sunlight illuminated targets compared to that observed with the ICU lamp and for comparing the spectral profile of stray light generated by targets when illuminated by sunlight to that obtained with sources at lower color temperatures (down to 80 °C with the internal blackbody).

IV. ADJUSTMENTS DUE TO POST-LAUNCH EVOLUTION AND IMPLEMENTATION IN THE MAJIS DATA PIPELINE

A. Post-launch evolution

Observations with the MAJIS ICU were performed during near-Earth commissioning to evaluate possible evolutions after launch (April 14, 2023). They showed that the overall performance was in line with calibration results, but there were small changes, which will require adjusting radiometric calibration results before implementing them as part of the MAJIS pipeline. Small shifts have been observed in the spectral direction for both the VISNIR and IR channels.[4] The impact on the ITF is minor in the spectral direction when considering the ICU spectra before and after launch (see Fig. 47).

The post-launch evolution is more significant in the spatial direction, as the signals with both ICU sources (blackbody and lamp) are lower at the left edge of the FOV and slightly higher at the right edge of the FOV than during calibration (see Fig. 48).

As this evolution after launch is similar for both channels, the cause of this change is upstream of the beam splitter. As performance is not markedly impacted, the most likely interpretation is that the relationship between the diffusing screen and the sources has changed, possibly due to a small rotation/deformation of the diffusive screen.

A small shift has also been observed in the spatial direction after launch when observing the ICU lamp with both the IR and VISNIR channels.[3] The left edge of the FOV as observed by the VISNIR channel has shifted right by 3.6 pixels (18 μm) after launch, while it has shifted left by 2.34 pixels (18 μm) for the IR channel. During calibration, there was already a mismatch with the left edge of the VISNIR FOV ~7–8 pixels (depending on wavelength) to the right of the IR FOV. After launch, this mismatch has increased to ~12 pixels (18 μm).

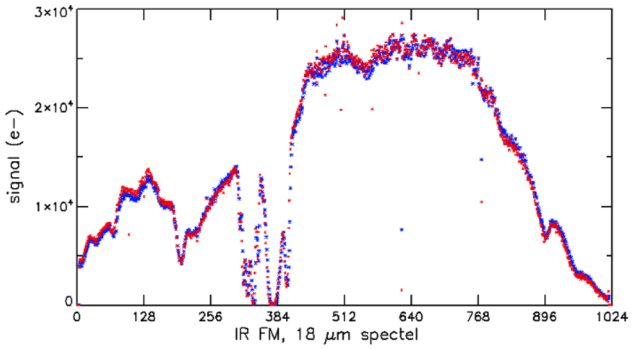

FIG. 47. Signal with the ICU blackbody source for pixel 400 of the IR channel during calibration (blue) and after launch (red).

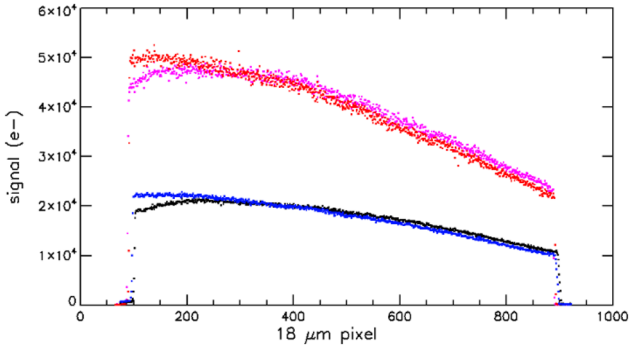

FIG. 48. Spatial profiles of the ICU lamp observed with the IR channel (spectel 101) during calibration (red) and after launch (magenta) and the VISNIR channel (spectel 700) during calibration (black) and after launch (blue).

These shifts in the position of the FOV as observed with the VISNIR and IR channels require adjusting the ITF-2D for both channels. The first issue is that the ITF-2D for the IR channel was directly evaluated from flat fields (Sec. III B) so that it included the variations of the transmission efficiency of the slit as positioned on the FPA during calibration.

The very good correlation in Fig. 49 demonstrates that the shift observed for the edges of the FOV (3.6 pixels to the right for the VISNIR and 2.3 pixels to the left for the IR) also applies to small high spatial frequency variations of the effective slit transmission (which apply to both channels). The IR 2D ITF determined during calibration must therefore be corrected by the ratio between the slit transmission applicable after launch and that which was applicable during calibration as derived from the ICU signal (Fig. 50). The left edge of the FOV shifts by ~2 pixels from spectel 100 (pixel 88) to spectel 900 (pixel 90) due to the slight tilt of the FPA with respect to the slit[3] so that this ratio depends on wavelength. Furthermore, there are three IR pixels (88, 89, and 90) now in the FOV, which had much lower signals when observing calibration sources. The IR 2D ITF will have to be extended to these pixels by combining the

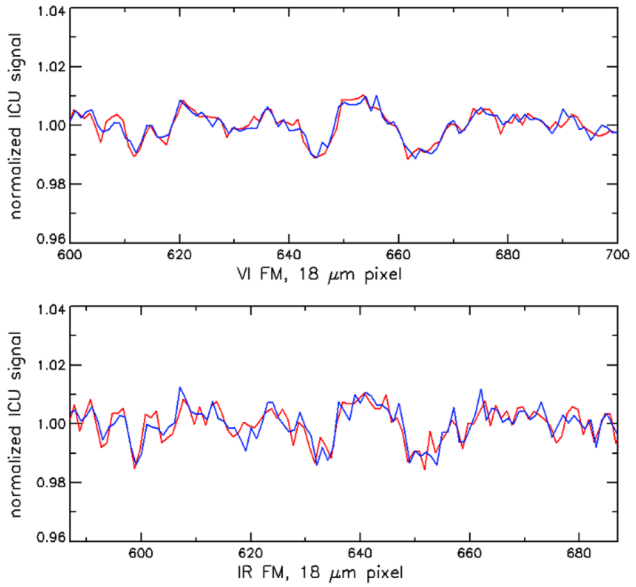

FIG. 49. Top panel: Normalized signal from the ICU lamp, median of VISNIR spectels 770–830 after launch (blue line) and before launch, shifted right by 3.6 pixels (red line). Bottom panel: Median of IR spectels 70–130, after launch (blue line) and before launch, shifted left by 2.3 pixels (red line). The IR pixel range (587–687) has been set to match that observed by VISNIR pixels 600–700 considering the shift of 12 pixels between the two channels after launch.

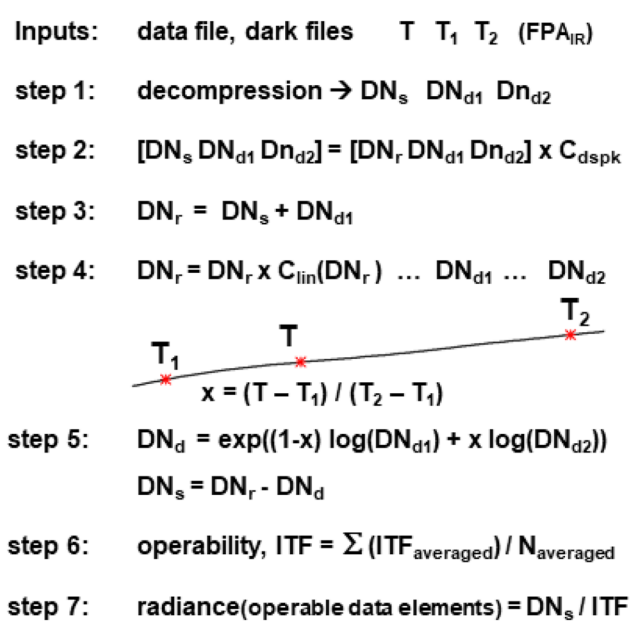

FIG. 50. MAJIS pipeline procedure for determining the radiance for each MAJIS data element. DN_r is the raw DN level, DN_{d2} and DN_{d1} are the DN levels for the dark before (1) and after (2) acquisitions, DN_s is the DN level after dark subtraction. C_{dspk} and C_{lin} are the correction coefficients to be applied for de-spiking and linearity (see the text).

inter-pixel variability of these three detector rows as derived from the characterization of the IR FM detector with the best estimate of the effective slit transmission at that location after launch.

For the VISNIR channel, as discussed in Secs. II and III C, the inter-pixel variability is smaller than for the IR channel and the 2D ITF is derived from the ITF in the center of the field by estimating low spatial frequency evolutions of the spectral response from flat sources and applying the high frequency variations due to the slit. The same approach can be used with ICU lamp observations to derive a 2D ITF applicable to post-launch VISNIR data. If further shifts of the FOV are observed with the ICU source during cruise or once at Jupiter, they will have to be considered for adjusting the 2D ITFs to be applied to VISNIR and IR data.

B. Implementation of the radiometric calibration results in the MAJIS data pipeline

Nominal MAJIS observations implement dark subtraction and data compression. Dark subtraction requires that two dark acquisitions are available before and after the observation as temperature evolutions are expected to be monotonous close to icy moons ("hot case") when the IR FPA dark current evolution could be significant. Implementing radiometric calibration as derived from Sec. III and adjusted for post-launch evolution (Sec. IV) to convert flight data into radiances requires the following steps to be taken in the MAJIS pipeline (Fig. 50):

(1) Decompression: Flight data can be sent either uncompressed or reversibly compressed after a shift S to the right by 0–7 bits. For each observation, the shift parameter is selected independently for up to 32 spectral ranges (16 for the VISNIR channel and 16 for the IR channel). DN levels will be adjusted for this shift according to Eq. (3), where DN_d is the DN value after decompression,

$$DN = (DN_d + 0.5) \times 2^S. \quad (3)$$

Dark signals before and after observations are sent uncompressed (S = 0).

(2) De-spiking compensation: The de-spiking procedure[19] averages 1–8 values from a series of sub-integrations. However, the proximity electronics performs this averaging by dividing by the next power of 2 for optimal performance. Therefore, averaging 3, 5, 6, or 7 values results in a DN value, which is multiplied by a factor of 3/4, 5/8, 6/8, or 7/8. This needs to be compensated in the pipeline on the basis of the de-spiking parameters, which are defined independently for the VISNIR and IR channels in the configuration TC for a given observation. The same de-spiking correction factor needs to be applied to the dark signal sent as uncompressed data before an observation as de-spiking has been applied for each of the nine acquisitions with the shutter closed on which basis the dark signal is evaluated. Further averaging steps are implemented by the compression units (spectral and/or spatial averaging by 1, 2, or 4, frame averaging),[1] but they maintain

the dynamics by dividing by the actual number of averaged values after summing them.

(3) Recovery of the raw DN level for each data element by adding back the "dark before" the DN level, which has been subtracted on the fly by the proximity electronics (both are real numbers at this stage).

(4) Linearity correction: The raw DN levels for the observation, the dark before and the dark after acquisitions must be corrected for linearity using tables relevant to MAJIS DNs (see Sec. II).

(5) Dark subtraction after adjusting for a possible evolution of the dark signal to be subtracted due to a temperature evolution of the IR FPA. Adjusting the dark signal only applies to the IR data, as the VISNIR dark signal is so low that its temperature dependence is irrelevant. For each data element, the "dark before" and "dark after" DN levels corrected for de-spiking and linearity are interpolated on the basis of the temperature of the IR FPA for each frame compared to that of the IR FPA at the time of the two bracketing dark signal acquisitions. The interpolation is performed on a log scale in line with the evolution of the dark current as a function of temperature. The result is subtracted from the raw DN level after step 4. Following this procedure is critical for achieving both precision and accuracy.[8] Additional corrections may be required at wavelengths larger than 4.5 μm, where the thermal background becomes significant, as it depends on the OH temperature, not on the IR FPA temperature. However, the thermal background signal smoothly varies with the position along slit and the wavelength so that a slightly off thermal background subtraction will not impact the identification of spectral features.

(6) Operability and determination of the relevant 2D ITFs: Depending on the spatial averaging and spectral averaging parameters in the configuration TC, a MAJIS data element averages from two detector pixels (spectral oversampling and no spatial binning) to 64 detector pixels (spectral and spatial binning by 4). The location of these pixels on the detector is defined by the "start pixel" parameter in the spatial direction and by the spectral averaging parameters of the configuration TC in the spectral direction. The first step consists in raising a non-operability flag is raised if any of the contributing detector pixels is flagged as non-operable depending on the FPA temperature and the integration time (this conservative approach could be reconsidered after testing for data elements averaging a large number of detector pixels). The operability of the VISNIR detector depends only weakly on detector temperature, the integration time, and the signal level (see Sec. II E) so that a single operability mask can be used for the 1016 × 1016 connected 18 μm pixels, which will be updated for additional dead, hot, or unreliable pixels on the basis of observations of the internal calibration unit. Due to spillover (see Sec. II E), the operability mask to be used for the IR channel depends on detector temperature, integration time, and signal level. Once non-operable data elements have been flagged as such, the 2D ITF to be applied for each channel is obtained for each operable data element by averaging the 2D ITF of its constituent detector pixels (VISNIR or IR, 1 MHz or 100 kHz) as determined in Sec. III and adjusted in Sec. IV, expressed in DNs per unit of radiance. It can be derived from the ITF presented in Fig. 28 for the IR channel and in Fig. 29 for the VISNIR channel (in e^- per unit of radiance) by considering the conversion coefficient in e^-/DN from Table II multiplied with a factor of 2 due to the shift right by 1 implemented by the MAJIS PE.

(7) The de-spiking corrected, linearity corrected, and dark subtracted DN levels of operable data elements in each frame of an observation can then be converted into radiances by dividing them by the 2D ITF relevant for the observation and channel.

V. CONCLUSIONS

The two-step process, which was implemented for the MAJIS radiometric calibration (characterization of the FM detectors and calibration of the integrated instrument), made it possible to investigate in depth the relationship of the MAJIS signal with the incoming radiance.

The correction for linearity, which had been determined during characterization, has been validated by the comprehensive set of observations performed during calibration over the full range of operational temperatures of the MAJIS VISNIR and IR detectors. The instrument transfer functions, which have been defined for converting MAJIS dataset into spectral radiances, also apply to all operating temperatures, with the exception of wavelengths longer than 5100 nm (IR channel) for which a correction will need to be applied when the temperature of the IR FPA exceeds 96 K ("hot case") due to a decrease in the cutoff wavelength. An important result of characterization has been to demonstrate that a series of MAJIS data acquisitions are free of persistence, thereby validating the on-board de-spiking procedure selected for MAJIS,[19] which should be effective even in "hot" radiative environments such as the two Europa flybys.

The overall performance in terms of signal levels and SNR meets or exceeds requirements over the full wavelength range of MAJIS (see Ref. 1). This is in particular the case for the capability to detect very low signals, on which basis H1RG detectors had been selected for both channels of MAJIS. Calibration results at the blue edge of Planck radiances have showed that by using a specific readout approach associated with dark signal subtraction, MAJIS should be able to reliably evaluate signal levels in the range of 5 e^- with a single acquisition, less with stacking.

The main issue with an impact on the interpretation of MAJIS data is a stray light contribution in the VISNIR channel, which represents a major fraction of the signal from calibration sources for wavelengths smaller than 1300 nm. Specific procedures had to be implemented so as to determine the instrument transfer function for the legitimate signal in this spectral range. The stray light contribution is much smaller at wavelengths larger than 1300 nm, but it still has a major impact in the upper end of the wavelength range of the VISNIR channel (2250–2370 nm) where the legitimate contribution drops to very low levels. A stray light issue was also identified at the low end of the IR wavelength range when using radiances from a blackbody at temperatures ranging from −80 to +50 °C for radiometric calibration. This issue will not impact science acquisitions as stray light was not observed in the IR with bluer sources; hence, this will also be the case for sunlit targets.

An analysis of the origin of the VISNIR stray light has led to the conclusion that the loss in spectral contrast due to this contribution should not exceed ~10% at the center of the FOV (worst case) for sunlit targets. This needs to be confirmed by observations of the Moon, with a first opportunity in August 2024. If this is the case, the impact on the science objectives associated with the wavelength ranges with significant levels of stray light should be relatively minor, as the identification of specific spectral features will still be possible with a slightly reduced spectral contrast except in a narrow wavelength range (600–700 nm). A small subset of the early observations of Jupiter and icy moons will be performed with a readout extending beyond the FOV so as to evaluate the corresponding stray light levels (see Sec. III C) and their possible impact on the science objectives relying on VISNIR data.

As discussed in Sec. IV, a post-launch evolution has been detected using data from the internal calibration unit (ICU), with a small spectral and spatial shift for both the VISNIR and IR channels. The high SNR with the ICU lamp made it possible to determine the small adjustments (at the % level) to be made on the two-dimensional instrument transfer functions determined during calibration for implementation on post-launch data in the MAJIS data pipeline. The ICU data also showed that the performance in terms of spatial and spectral resolution is similar to that evaluated during calibration.[3,4] The evolution of the performance will continue to be monitored using the ICU lamp and the ICU blackbody, which provides adequate SNR up to the upper end of the IR wavelength range, during cruise and science operations in orbit around Jupiter and Ganymede. The procedure validated with the post-launch evolution will make it possible to update the transfer functions if further evolutions are identified. An update will also be required for operability maps on the basis of ICU data, as additional 18 μm pixels are likely to be degraded by high energy particles in the environment of Jupiter until the end of the nominal JUICE science mission (September 2035).

ACKNOWLEDGMENTS

The French contribution to MAJIS has been technically supported and funded by CNES – CONTRACT CNES – CNRS under Grant No. 180 117. The Italian contribution to MAJIS has been coordinated and funded by Italian Space Agency under Contract No. 2021-18-I.0 and supported by the ASI-INAF Agreement No. 2023-6-HH.0.

AUTHOR DECLARATIONS

Conflict of Interest

The authors have no conflicts to disclose.

Author Contributions

Y. Langevin: Conceptualization (lead); Data curation (equal); Investigation (equal); Methodology (equal); Supervision (equal); Validation (equal); Writing – original draft (lead). **F. Poulet**: Data curation (supporting); Funding acquisition (lead); Investigation (equal); Supervision (lead); Validation (equal); Writing – review & editing (supporting). **G. Piccioni**: Funding acquisition (lead); Investigation (equal); Supervision (equal); Validation (equal). **G. Filacchione**: Conceptualization (equal); Data curation (equal); Investigation (equal); Validation (equal). **C. Dumesnil**: Funding acquisition (equal); Investigation (equal); Project administration (equal); Resources (equal); Supervision (equal). **F. Tosi**: Data curation (supporting); Methodology (equal). **J. Carter**: Data curation (equal); Investigation (equal); Validation (equal). **A. Barbis**: Data curation (equal); Investigation (equal); Methodology (equal). **P. Haffoud**: Data curation (equal); Investigation (equal); Validation (equal). **L. Tommasi**: Conceptualization (equal); Funding acquisition (equal); Investigation (equal); Project administration (equal); Resources (equal). **M. Vincendon**: Conceptualization (equal); Investigation (equal); Methodology (equal). **S. De Angelis**: Data curation (equal); Investigation (equal). **I. Guerri**: Conceptualization (equal); Investigation (equal). **C. Pilorget**: Conceptualization (equal); Investigation (equal). **S. Rodriguez**: Data curation (equal); Investigation (equal). **S. Stefani**: Data curation (equal); Investigation (equal). **D. Bolsée**: Funding acquisition (equal); Investigation (equal); Methodology (equal); Supervision (equal). **M. Cisneros**: Data curation (equal); Investigation (equal); Validation (equal). **L. Van Laeken**: Data curation (equal); Investigation (equal); Validation (equal). **N. Pereira**: Conceptualization (equal); Investigation (equal); Methodology (equal). **A. Carapelle**: Conceptualization (equal); Funding acquisition (equal); Investigation (equal).

DATA AVAILABILITY

The data which were used for this article are available from the corresponding author upon reasonable request.

REFERENCES

[1] F. Poulet, G. Piccioni, Y. Langevin, C. Dumesnil, L. Tommasi, V. Carlier, G. Filacchione, M. Amoroso, A. Arondel, E. D'Aversa *et al.*, "Moons and Jupiter Imaging Spectrometer (MAJIS) on Jupiter Icy Moons Explorer (JUICE)," Space Sci. Rev. **220**, 27 (2024).

[2] M. Vincendon, P. Guiot, B. Lecomte, M. Condamin, F. Poulet, A. Arondel, J. Barbay, J. Carter, S. De Angelis, C. Dumesnil *et al.*, "Calibration of MAJIS (Moons and Jupiter Imaging Spectrometer): I. Calibration set-up," *Rev. Sci. Instrum.* (to be published).

[3] G. Filacchione, P. Haffoud, F. Poulet, G. Piccioni, Y. Langevin, L. Tommasi, A. Barbis, J. Carter, I. Guerri, C. Dumesnil *et al.*, "Calibration of MAJIS (Moons and Jupiter Imaging Spectrometer): II. Spatial calibration," Rev. Sci. Instrum. **95**, 041301 (2024).

[4] P. Haffoud, F. Poulet, M. Vincendon, G. Filaccione, A. Barbis, P. Guiot, B. Lecomte, Y. Langevin, G. Piccioni, C. Dumesnil *et al.*, "Calibration of MAJIS (Moons and Jupiter Imaging Spectrometer): III. Spectral calibration," Rev. Sci. Instrum. **95**, 031301 (2024).

[5] S. Rodriguez, M. Vincendon, P. Haffoud, Y. Langevin, F. Poulet, E. Quirico, C. Pilorget, J. Carter, R. Brunetto, B. Lecomte *et al.*, "Calibration of MAJIS (Moons and Jupiter Imaging Spectrometer): V. Validation with mineral samples and reference materials," Rev. Sci. Instrum. **95**, 101301 (2024).

[6] S. Stefani, G. Piccioni, F. Poulet, M. Vincendon, G. Filacchione, A. Barbis, P. Guiot, B. Lecomte, Y. Langevin, C. Dumesnil *et al.*, "Calibration of MAJIS (Moons and Jupiter Imaging Spectrometer): VI. The internal calibration unit (ICU)," *Rev. Sci. Instrum.* (submitted).

[7] B. J. Rauscher, O. Fox, P. Ferruit, R. Hill, A. Waczynski, Y. Wen, W. Xia-Serafino, B. Mott, D. Alexander, C. K. Brambora *et al.*, "Detectors for the *James Webb Space Telescope* near-infrared spectrograph. I. Readout mode, noise model, and calibration considerations," Publ. Astron. Soc. Pac. **119**, 768–786 (2007).

[8] A. Secroun, R. Barbier, C. Buton, J.-C. Clémens, L. Conversi, A. Ealet, S. Ferriol, F. Fornari, W. Gilard, R. Kohley *et al.*, "Euclid flight H2RG IR detectors: Per pixel conversion gain from on-ground characterization for the Euclid NISP instrument," Proc. SPIE **10709**, 1070921 (2018).

[9]M. Loose, J. Beletic, J. Garnett, and M. Xu, "High-performance focal plane arrays based on the HAWAII-2RG/4G and the SIDECAR ASIC," Proc. SPIE **6690**, 66900C (2007).
[10]R. Blank, S. Anglin, J. W. Beletic, S. Bhargava, R. Bradley, C. A. Cabelli, J. Chen, D. Cooper, R. Demers, M. Eads *et al.*, "H2RG focal plane array and camera performance update," Proc. SPIE **8453**, 845310 (2012).
[11]M. Brown, M. Schubnell, and G. Tarle, "Correlated noise and gain in unfilled and epoxy-underfilled hybridized HgCdTe detectors," Publ. Astron. Soc. Pac. **118**, 1443–1447 (2006).
[12]S. Seshadri, D. M. Cole, B. R. Hancock, and R. M. Smith, "Mapping electrical crosstalk in pixelated sensor arrays," Proc. SPIE **7021**, 702104 (2008).
[13]Y. Langevin, V. Carlier, C. Hannou, L. Gonnod, J. Carter, F. Tosi, G. Filacchione, C. Dumesnil, G. Piccioni, and F. Poulet, "H1RG readout procedures for MAJIS, the VIS/NIR imaging spectrometer of JUICE: Impacts on the performances," Proc. SPIE **12180**, 1218037 (2022).
[14]D. Bolsée, L. Van Laeken, M. Cisneros-González, N. Pereira, C. Depiesse, L. Jacobs, A.-C. Vandaele, B. Ritter, S. Gissot, O. Karatekin *et al.*, "Characterization facility for the MAJIS/JUICE VIS-NIR FM and SM detectors," Proc. SPIE **11443**, 114437H (2020).
[15]M. Cisneros-González, D. Bolsée, N. Pereira, L. Van Laeken, C. Depiesse, L. Jacobs, S. Robert, A.-C. Vandaele, S. Gissot, O. Karatekin *et al.*, "MAJIS/JUICE VIS-NIR FM and SM detectors characterization," Proc. SPIE **11443**, 114431L (2020).
[16]J. Carter, P. Haffoud, Y. Langevin, F. Poulet, C. Ketchazo, P. Guiot, C. Dumesnil, C. Ruiz de Galarreta Fanjul, A. Arondel, V. Carlier *et al.*, "MAJIS IR channel: 3) performance of the focal plane unit," Proc. SPIE **12180**, 121803A (2022).
[17]P. Haffoud, A. Arondel, D. Bolsée, V. Carlier, J. Carter, M. Cisneros-Gonzalez, J.-P. Dubois, C. Dumesnil, G. Filacchione, L. Gonnod *et al.*, "MAJIS VIS-NIR channel: Performances of the focal plane unit - flight model," Proc. SPIE **12180**, 1218039 (2022).
[18]P. Guiot, M. Vincendon, J. Carter, Y. Langevin, and A. Carapelle, "Characterization of transient signal induced in IR detector array by Jupiter high-energy electrons and implications for JUICE/MAJIS operability," Planet. Space Sci. **181**, 104782 (2020).
[19]Y. Langevin, M. Zambelli, and P. Guiot, "On-board de-spiking implemented by MAJIS, the VIS/NIR imaging spectrometer of JUICE," Proc. SPIE **11443**, 1144378 (2020).
[20]A. Barbis, M. Barilli, A. Bini, M. Dami, E. Fossati, G. Pilato, L. Tommasi, G. Filacchione, S. De Angelis, G. Piccioni *et al.*, "MAJIS/JUICE optical head: Characterization campaign and derived performance test results," Proc. SPIE **12180**, 121800G (2022).
[21]J. Carter, X. Zhang, B. Lecomte, C. Ruiz de Galarreta Fanjul, P. Haffoud, A. Arondel, R. Brunetto, J. P. Dubois, C. Dumesnil, Y. Langevin, G. Morinaud, and F. Poulet, "MAJIS focal plane unit: Performance of the IR channel filters," Proc. SPIE **12180**, 1218038 (2022).
[22]G. L. Hansen, J. L. Schmit, and T. N. Castelmann, "Energy gap versus alloy composition and temperature in $Hg_{1-x}Cd_xTe$," J. Appl. Phys. **53**, 7099 (1982).